

1 Revision #1 submission to *American Mineralogist*, centennial edition, Mars mineralogy, special
2 section

3 Submitted: 30 Sept. 2015; Resubmitted: 15 February 2016

4

5 **Discovery of Alunite in Cross Crater, Terra Sirenum, Mars: Evidence for Acidic, Sulfurous**
6 **Waters**

7 Bethany L. Ehlmann^{1,2,*}, Gregg A. Swayze^{3,*}, Ralph E. Milliken⁴, John F. Mustard⁴, Roger N.
8 Clark⁵, Scott L. Murchie⁶, George N. Breit³, James J. Wray⁷, Brigitte Gondet⁸, Francois Poulet⁸,
9 John Carter⁸, Wendy M. Calvin⁹, William M. Benzel³, Kimberly D. Seelos⁶

10

11 ¹Division of Geological & Planetary Sciences, California Institute of Technology, Pasadena,
12 California, 91125, USA. Email: ehlmann@caltech.edu

13 ²Jet Propulsion Laboratory, California Institute of Technology, Pasadena, California, 91109,
14 USA

15 ³U.S. Geological Survey, Denver, Colorado, 80225, USA

16 ⁴Department of Earth, Environmental, & Planetary Sciences, Brown University, Providence,
17 Rhode Island, 02906, USA

18 ⁵Planetary Science Institute, Tucson, Arizona, 85719, USA

19 ⁶Johns Hopkins University, Applied Physics Laboratory, Laurel, Maryland, 20723, USA

20 ⁷School of Earth & Atmospheric Sciences, Georgia Institute of Technology, Atlanta, Georgia,
21 30332, USA

22 ⁸Institut d'Astrophysique Spatiale, Université Paris-Sud, Orsay, 91405, France

23 ⁹Department of Geological Sciences, University of Nevada, Reno, Nevada, 89557, USA

24 *These authors contributed equally to this work

25

26 **Keywords:** alunite, phyllosilicates, hydrothermal activity, lakes, groundwater, Mars, sediments,
27 infrared spectroscopy

28

29
30
31
32
33
34
35
36
37
38
39
40
41
42
43
44
45
46
47
48
49
50
51
52

Abstract

Cross crater is a 65-km impact crater, located in the Noachian highlands of the Terra Sirenum region of Mars (30°S, 158°W), which hosts aluminum phyllosilicate deposits first detected by the Observatoire pour la Minéralogie, L'Eau, les Glaces et l'Activité (OMEGA) imaging spectrometer on Mars Express. Using high resolution data from the Mars Reconnaissance Orbiter, we examine Cross crater's basin-filling sedimentary deposits. Visible/shortwave infrared (VSWIR) spectra from the Compact Reconnaissance Imaging Spectrometer for Mars (CRISM) show absorptions diagnostic of alunite. Combining spectral data with high resolution images, we map a large (10 km x 5 km) alunite-bearing deposit in southwest Cross crater, widespread kaolin-bearing sediments with variable amounts of alunite that are layered in <10-m scale beds, and silica- and/or montmorillonite-bearing deposits that occupy topographically lower, heavily fractured units. The secondary minerals are found at elevations ranging from 700 to 1550 m, forming a discontinuous ring along the crater wall beneath darker capping materials. The mineralogy inside Cross crater is different from that of the surrounding terrains and other Martian basins, where Fe/Mg-phyllosilicates and Ca/Mg-sulfates are commonly found. Alunite in Cross crater indicates acidic, sulfurous waters at the time of its formation. Waters in Cross crater were likely supplied by regionally upwelling groundwaters as well as through an inlet valley from a small adjacent depression to the east, perhaps occasionally forming a lake or series of shallow playa lakes in the closed basin. Like nearby Columbus crater, Cross crater exhibits evidence for acid sulfate alteration, but the alteration in Cross is more extensive/complete. The large but localized occurrence of alunite suggests a localized, high volume source of acidic waters or vapors, possibly supplied by sulfurous (H₂S- and/or SO₂-bearing) waters in contact with a magmatic source, upwelling steam or fluids through fracture zones. The unique, highly aluminous nature of the Cross crater deposits relative to other Martian acid sulfate deposits

53 indicates acid waters, high water throughput during alteration, atypically glassy and/or felsic
54 materials, or a combination of these conditions.

55

56

Introduction

57 Although geomorphic evidence for the presence of liquid water on Mars has been
58 longstanding (e.g. Carr, 1996 and refs. therein), mineralogic evidence for aqueous alteration of
59 rocks on the Martian surface has been revealed relatively recently by in-situ exploration by the
60 Mars Exploration Rovers (MER; e.g., Squyres et al., 2004a,b; 2008; Arvidson et al., 2006) and
61 by high resolution, orbital infrared spectroscopy. Thermal Emission Spectrometer (TES) data
62 (Christensen et al., 2001), Thermal Imaging System (THEMIS) data (Christensen et al., 2004;
63 Osterloo et al., 2008), and visible shortwave-infrared (VSWIR) imaging spectrometer data from
64 the Observatoire pour la Minéralogie, L'Eau, les Glaces et l'Activité (OMEGA) on Mars
65 Express (Bibring et al., 2005) and the Compact Reconnaissance Imaging Spectrometer for Mars
66 (CRISM) onboard the Mars Reconnaissance Orbiter (MRO; Murchie et al., 2007) have revealed
67 sulfates, carbonates, chlorides, phyllosilicates, and other hydrated silicates on the surface of Mars
68 (e.g., Gendrin et al., 2005; Poulet et al., 2005; Bibring et al., 2006; Mustard et al., 2008; Osterloo
69 et al., 2008; Ehlmann et al., 2008; Murchie et al., 2009a). Salts and secondary minerals indicative
70 of water are heterogeneously distributed. Whereas phyllosilicates are widespread and distributed
71 globally in Noachian and some Hesperian terrains, salts such as chlorides, carbonates, and
72 sulfates show more restricted and spatially distinct geographic distributions (e.g., Ehlmann &
73 Edwards, 2014). Few hydrated minerals are mapped in Amazonian terrains (e.g. Bibring et al.,
74 2006; Carter et al., 2013). Distinctive Martian geochemical environments characterized by
75 different pH, water:rock ratio, and fluid chemistry can thus be inferred. The geologic settings of
76 these salt- and secondary mineral-bearing units vary and include deltaic deposits, basin-filling
77 layered deposits, impact ejecta, and massive units that lack clear bedding.

78 Here, we report the geologic context and environmental implications of the first detection
79 on Mars of alunite, $\text{KAl}_3(\text{SO}_4)_2(\text{OH})_6$, using diagnostic shortwave-infrared absorptions in

80 CRISM data (after Swayze et al., 2008). In contrast to calcium and magnesium sulfates, which
81 are the predominant sulfates detected on Mars by orbital and surface data (e.g. Gendrin et al.,
82 2005; Murchie et al., 2009a; Vaniman et al., 2014), alunite is rare and found to date only in the
83 Terra Sirenum region (Swayze et al., 2008; Wray et al., 2011). Alunite is an indicator of
84 distinctly acidic geochemical conditions during precipitation, pointing to low pH, sulfurous
85 fluids at or near the Martian surface. We examine the mineral assemblages, their
86 geomorphology, and regional context to understand the controls on spatially extensive alunite
87 formation in Cross crater and the environmental setting(s) of aqueous alteration.

88 **Datasets & Methods**

89 Cross crater, a 65-km-diameter late-Noachian impact crater in the southern highlands of
90 Terra Sirenum (30°S, 158°W; Figure 1), was targeted by MRO based on an absorption at 2.2 μm
91 seen in a few pixels of OMEGA data, which suggested the presence of an Al-phyllsilicate such
92 as kaolinite (Gondet et al., 2006). Cross crater is west of the Tharsis rise volcanic edifice in a
93 faulted area with several candidate closed basin lakes (Anderson et al., 2001; Goudge et al.,
94 2015). Seventeen CRISM images were acquired over Cross crater in 544 spectral channels from
95 0.4-3.9 μm in full-resolution targeted mode, covering approximately 10 x 10 km with a spatial
96 sampling of 18-20 m/pixel, and in half-resolution mode targeted mode, covering 10 x 20 km with
97 a spatial sampling of 35-40 m/pixel (Murchie et al., 2007) (Table 1). In targeted mode, CRISM's
98 effective spectral resolution near 2.2 μm is approximately 10 nm, allowing narrow SWIR
99 absorptions such as the 2.2- μm doublet present in kaolinite group minerals to be resolved.
100 Analyses of data from 0.4-2.6 μm enable identification of minerals using diagnostic electronic
101 absorptions in the visible and shortwave infrared (VSWIR) from transition metals such as iron as
102 well as vibrational absorptions from OH, H₂O, and CO₃. Additionally, CRISM data were
103 acquired in multispectral mapping mode over the same wavelength range but with decreased

104 spatial and spectral resolution (Murchie et al., 2007; 2009b). VSWIR remote sensing data
105 measure the composition of the upper hundreds of micrometers of the surface; consequently,
106 determination of the mineralogy of lithologic/stratigraphic units requires the bedrock be at least
107 patchily exposed beneath other surface covers, e.g. dust, sand, or overlying units.

108 Raw CRISM spectra were processed to I/F (a ratio of measured radiance to incoming
109 solar flux) following the methodology of Murchie et al. (2009b) and were then photometrically
110 and atmospherically corrected using standard procedures. Assuming a surface that scatters
111 isotropically, i.e., a Lambertian surface, scene I/F was divided by the cosine of the incidence
112 angle, and then corrected for atmospheric gas band absorptions by dividing by a scaled
113 atmospheric transmission spectrum (e.g., Mustard et al., 2008; Ehlmann et al., 2009). To
114 highlight spectral features that differ between terrains and to reduce the effect of systematic,
115 detector-dependent instrument artifacts, individual or average spectra from areas of interest were
116 ratioed to an average spectrum of areas located within the same image column and lacking
117 narrow vibrational absorptions. Spectral summary parameters (Pelkey et al., 2007), which
118 spatially map the strength of absorptions related to Fe, OH, and H₂O at locations diagnostic of
119 minerals and mineral classes were used initially to discover and detect minerals of interest.

120 The locations of minerals with diagnostic infrared absorptions were also mapped using
121 the Tetracorder spectral shape-matching algorithms and expert system (Clark et al., 2003),
122 coupled with the Clark et al. (2007) spectral library, to create color-coded maps of the
123 distribution of minerals and/or spectral endmembers with absorptions in the 1.0-2.6 μm range.
124 Tetracorder compares absorption features in library reference spectra to absorption features in an
125 observed spectrum (e.g., in a CRISM pixel) and then calculates the modified least-squares
126 correlation between them. The algorithm derives a fit (a correlation coefficient) for each of the

127 spectra in its library, applies user-specified constraints on absorption features, and selects the
128 mineral with the highest fit as the best spectral match to the observed spectrum. Maps of the
129 distribution of various minerals are assembled by assigning a unique color to pixels spectrally
130 dominated by a particular mineral or mineral mixture.

131 CRISM parameter and Tetracorder mineral maps were then map projected and co-
132 registered with MRO high spatial resolution image data collected at 6 m/pixel by the Context
133 Imager (CTX; Malin et al., 2007) and at 0.3 m/pixel by the High Resolution Imaging Science
134 Experiment (HiRISE; McEwen et al., 2007). HiRISE red-blue anaglyphs and digital elevation
135 models provided high resolution topographic information at 1 m/pixel for one location where
136 stereo image pairs were available. Topography at larger scales was determined using 128
137 pixel/degree Mars Orbiter Laser Altimeter (MOLA) global gridded data as well as point shot
138 data acquired with a ~168 m diameter spot-size at ~300 m spacing with an absolute vertical
139 precision of ~38 cm and accuracy of ~1 m (Smith et al., 2001). Additional daytime and nighttime
140 infrared images from the Thermal Emission Imaging System (THEMIS) mosaics provided
141 context for the high-resolution datasets as well as insight into the thermophysical properties of
142 the geologic materials (e.g., Fergason et al., 2006; Edwards et al., 2011).

143 **Results**

144 Cross crater hosts a diverse suite of secondary and primary minerals found in discrete
145 geomorphic units. Sedimentary units, mostly restricted to elevations between 700 m and 1550 m,
146 contain kaolinite group phyllosilicates and certain locales have alunite, silica and/or
147 montmorillonite, Fe/Mg-phyllosilicates, Fe-oxides, and Fe-sulfates. These units are overlain by
148 unconsolidated sediment (sands) as well as a lithified capping unit with weak SWIR absorptions

149 indicative of pyroxene group minerals. The details of the composition inferred from
150 spectroscopy, the geomorphology, and the distribution of key units are described below.

151 **Alunite, Al-phyllsilicates, silica**

152 Three endmember materials have absorptions near 2.2 μm , exhibit consistent and
153 distinctive spectral characteristics (red, blue, green spectra in Figure 2), display spatial coherence
154 when mapped in CRISM images, and occur in multiple localities in different CRISM images
155 (Figure 3). Along the southwestern wall, a ~ 10 km light-toned deposit occurs within a 860-1020
156 m elevation topographic contour and has a distinctive absorption at 2.17 μm , accompanied by a
157 doublet near 1.4 μm and absorptions at 1.76 μm , 2.32 μm , and 2.52 μm . These absorptions are
158 uniquely characteristic of alunite group minerals ($(\text{K}, \text{Na}, \text{H}_3\text{O})\text{Al}_3(\text{SO}_4)_2(\text{OH})_6$) (Figures 2; Hunt
159 et al. 1971; Clark et al., 1990; Swayze, 1997; Bishop and Murad, 2005). The difference between
160 K-bearing alunite and Na-bearing natroalunite is resolvable at CRISM spectral resolution
161 (Swayze, 1997; Bishop & Murad, 2005; Swayze et al., 2006, 2014; McCollom et al., 2014).
162 CRISM spectra of the Cross crater deposit have absorptions at 1.43 and 1.48 μm , which are
163 consistent with alunite, whereas natroalunite has longer wavelength absorptions near 1.44 and
164 1.49 μm , which are not observed. The presence of a 1.9- μm H_2O combination absorption and the
165 relative weakness and shapes of the ~ 1.4 - μm absorptions may be evidence for a poorly
166 crystalline alunite and incorporation of non-stoichiometric water (e.g., Swayze et al., 2006).
167 Mixtures of well-crystalline alunite with another hydrated phase can also generate these spectral
168 characteristics. Alunite-kaolinite mixtures are observed in other locations at 18 m/pixel
169 observation scale (yellow; Figures 2, 3).

170 The second and most widely occurring endmember with a ~ 2.2 - μm absorption, found in
171 every CRISM image of Cross crater floor sediments are kaolinite group minerals (referred to
172 collectively as kaolins). These have a pronounced asymmetry in their ~ 2.2 μm absorption, which

173 is due to differences in the relative strengths of the Al-OH doublet absorptions at 2.17 and 2.21
174 μm (Hunt 1977 and references therein; Clark et al., 1990; Bishop et al., 2008; Swayze et al.,
175 2014). A similar asymmetry in the weaker 1.41 μm absorption due to the Al-OH overtone can
176 also sometimes be resolved. The doublet is not pronounced in the Cross crater materials. As is
177 the case with other kaolin-bearing materials on Mars (e.g., Ehlmann et al., 2009), there is a 1.9-
178 μm absorption due to water that is not typical of well-crystalline, pure kaolinite, but is present in
179 halloysite, mixed-layer kaolinite-smectite clay, impure/disordered kaolinite, or kaolinite
180 physically mixed with hydrated phases. The breadth of the 2.21- μm absorption is also notably
181 wider than endmember spectral library kaolinite group minerals (Figure 2), indicating the kaolin-
182 bearing phase is likely areally or intimately mixed with other hydroxylated phases, such as
183 montmorillonite, hydrated silica, or alunite at the spatial resolution of CRISM.

184 The third endmember has a 2.2- μm absorption, also centered near 2.21 μm , which lacks
185 the asymmetry of kaolinite group minerals and is substantially broader. The center position and
186 lack of a doublet are characteristic of an Al-smectite phase like montmorillonite or an opaline
187 silica phase, with the absorption caused by Al-OH or Si-OH respectively. The width of the
188 absorption makes opaline silica the most plausible single phase to explain the spectral
189 characteristics; however, mixture of a montmorillonite with opaline silica or another phase, could
190 also cause apparent broadening of the 2.2- μm absorption.

191 **Iron mineralogy**

192 Fe/Mg-phyllsilicates, the most common phyllosilicate on Mars (e.g., Carter et al., 2013;
193 Ehlmann & Edwards, 2014), are uncommon within Cross crater and found so far only in the
194 west, in the vicinity of a small impact crater that impacts Cross crater floor units (Figure 4). In
195 contrast, multiple localities with Fe/Mg-phyllsilicates are located in the Noachian plateau unit
196 into which Cross crater was emplaced (e.g., Figure 1d; Figure 4b). The absorptions due to

197 Fe/Mg-phyllsilicates within Cross crater are centered near 1.43 μm , 1.9 μm , and 2.29 μm ,
198 consistent with an Fe-rich smectite such as nontronite (Figure 4c; Bishop et al., 2002a,b).
199 Outside of Cross crater on the plateau, the terrains have only been observed by CRISM using its
200 multispectral mapping mode so the spectral resolution for discriminating absorption band
201 minima is lower. However, the composition may be different. Observed absorptions in the
202 Fe/Mg phyllosilicate-bearing terrains near Cross crater are centered near 1.39 μm and $>2.30 \mu\text{m}$,
203 which may indicate a different, more Mg-rich, Fe/Mg-phyllsilicate chemical composition.

204 Within Cross crater and the alunite- and kaolin-bearing materials, CRISM spectra
205 acquired from 0.4-1.0 μm ('S data') exhibit variations in short wavelength spectral slope at 0.4-
206 0.9 μm . These may be due to the presence of iron oxides and/or iron sulfates within the deposits.
207 In CRISM spectral parameters, variation in dust cover is the primary cause of variability in the
208 0.53- μm band depth parameter rather than crystalline iron oxides; however, certain locations in
209 the sediments and the central ring knobs have absorptions that may indicate an Fe oxide phase.
210 In image FRT0001187B, there are also several small locations ($<250 \times 250 \text{ m}$) within the
211 alunite- and kaolin-bearing units with a 0.94- μm absorption. One of these has an atypically sharp
212 absorption at 2.22-2.23 μm , likely an indicator of $\text{Fe(III)SO}_4\text{OH}$, which has been previously
213 detected on Mars in Aram chaos (Lichtenberg et al., 2010) and in opal-bearing, light-toned
214 layered deposits adjacent to Valles Marineris (Milliken et al., 2008). Additionally, knobs that
215 have a yellow-brown tone in CRISM false-color IR images (R: 2.5 μm , G: 1.8 μm , B: 1.2 μm)
216 have a strong, positive spectral slope downward at wavelengths $<1.5 \mu\text{m}$, likely caused by one or
217 more Fe-bearing minerals. One small knob in FRT0000987B has spectra consistent with jarosite.
218 A follow-on paper will provide further small-scale geologic mapping of all alteration phases,
219 including iron sulfate phases within Cross crater sediments (Swayze et al., in prep.).

220 Spectral signatures of mafic minerals are uncommon within the crater, found only in
221 overlying sands and certain well-preserved outcrops of caprock. In some locales, the caprock has
222 discernible weak, broad absorptions centered near $\sim 0.9 \mu\text{m}$ and $\sim 2.1 \mu\text{m}$ that are consistent with
223 high-calcium pyroxene group minerals. Olivines and low-calcium pyroxenes are not obviously
224 present, although identification of mafic minerals is complicated by the fact the caprock is the
225 most “bland” material in the scene and thus the typical denominator used to remove residual
226 artifacts. There is variability from place to place in apparent pyroxene content, but the signatures
227 are subtle.

228 **Distribution and Geomorphology of Key Intracrater Units**

229 The alunite and Al-phyllosilicates are found in sediments ringing the crater floor,
230 typically exposed between a maximum elevation of approximately 1550 m above the MOLA
231 global datum and a minimum elevation of 700 m. Spatial mapping from Tetracorder analyses of
232 CRISM targeted data shows a concentration of pixels most closely matching spectrally dominant
233 alunite along the southwestern crater wall (Figure 5). Elsewhere, spectral signatures of kaolin-
234 bearing materials are spatially dominant, occurring solely or with variable intermixture of alunite
235 or opaline silica/montmorillonite.

236 A MOLA point shot profile across the largest spatially contiguous concentration of
237 dominantly alunite-bearing materials shows that the alunite- and kaolin-bearing materials are
238 part of a bench (Figure 5b). A break in slope at the transition from the crater wall to the bright-
239 toned sedimentary units suggests that these materials unconformably overlie the crater wall with
240 an upper surface that is nearly horizontal. The alunite is best expressed along the slope,
241 presumably exposed by modern wind erosion (Figure 5b, c). The dominantly alunite portion of
242 the sequence has a lighter-toned, more massive appearance than kaolin-bearing units, and lacks

243 clear bedding, fracturing or other obvious sedimentary structures (Figure 5d, e). The transition
244 from the alunite- and kaolin-bearing materials to the silica/montmorillonite coincides with
245 another break in slope and a change in deposit morphology (position #4 in Figure 5b,c). The
246 alunite- and kaolin-bearing units are massive to layered and form local topographic highs; the
247 silica/montmorillonite-bearing units are polygonally fractured at multiple scales and are
248 topographically lower. The silica/montmorillonite-bearing materials have prominent 500-2000 m
249 long cracks that are 10s of meters wide; buttes of dark caprock rest unconformably atop, in some
250 cases straddling these cracks (Figure 5f). Fracturing in this unit is also common at smaller scales
251 down to a few meters (Figure 5g).

252 Al-phylosilicate-bearing sedimentary units exposed in cross section are typically layered
253 at a scale of <5 m in thickness (Figure 6). Buttes of the alunite- and kaolin-bearing remnant
254 layers exist in all sectors of the crater, although coverage of stereo data acquired to date does not
255 yet permit tracing whether bed elevations are continuous across the crater. There are two
256 characteristic types of layering: (1) <5 m thick layers of bright and dark materials exposed on
257 relatively smooth-sloped, continuous scarps (Figure 6a, c) and (2) <10-m thick layers of
258 materials with homogeneous albedo properties but variable erodibility such that they form highly
259 irregular scarps with distinct breaks in slope between layers (Figure 6b). Type (2) are areally
260 dominant, especially in the northern part of the crater. Type (1) are rarer but are exposed in both
261 the north (Figure 6a) and in the south (Figure 6c). Notably, the alunite-bearing materials are not
262 associated with these most clearly layered terrains but rather with units with a distinctly massive
263 appearance (Figure 6d).

264 Overlying the sedimentary materials on the margins of the crater from an elevation of
265 700-800 m and extending to lower elevations, including the center of the crater, is a darker,

266 rougher looking cap rock unit that lacks a strong spectral signature in CRISM data but has some
267 characteristics indicative of the presence of high-Ca pyroxene group minerals. This dark unit,
268 which is <50-m thick and possibly considerably thinner, may be a coarse-grained sedimentary
269 unit, ash fall, or lava flow. Where removed by erosion, the underlying alunite-, kaolin-, and
270 silica/montmorillonite-bearing units are exposed (Figure 5e,f). Where the dark caprock is
271 preserved, its presence precludes determination of whether underlying aluminous units extend
272 across the entire basin. In addition to being atop the alunite-, kaolin-, and silica/montmorillonite-
273 bearing units, the dark caprock also embays central topographic highs that have a lower thermal
274 inertia, interpreted to be the peak ring structure of the crater. The dark capping material is
275 brightest in nighttime temperature data (Figure 1c), suggesting that it is the highest thermal
276 inertia material in the crater, which implies coarser grain size, greater cementation, and/or more
277 coherent bedrock relative to the other units.

278 The sole intracrater exposure of Fe/Mg-smectites is found in images FRT0000ACE6 and
279 FRT0000987B, covering an area southeast of a small impact crater, which excavates into
280 caprock and sediments in Cross crater. There is a small area with Fe-smectite in the impact
281 crater's rim in CRISM image FRT0000ACE6 (Figure 4a,c). Additional Fe-smectite deposits are
282 located approximately two crater-radii away from the small impact structure and are slightly
283 higher albedo in the infrared wavelengths than surroundings. Indistinctly layered materials in the
284 upper part of the stratigraphy are the likely host materials. There are some linear features radial
285 to the crater, indicating the presence of ejecta streamers; however, the majority of the small
286 crater's rim rock and ejecta do not have Fe/Mg-phyllsilicate signatures. Consequently, it is not
287 clear if the Fe-smectites are in the ejecta or in underlying materials scoured and exposed by the
288 ejecta. FRT00012E09 also may have spectra of Fe/Mg-smectites in a window beneath the

289 caprock, although the signature is weak, restricted to <10 pixels; and CTX resolution is
290 insufficient to resolve the morphology. Resolving the morphology and stratigraphy of the Fe/Mg
291 phyllosilicates in Cross crater will have to await acquisition of further CRISM and HiRISE data
292 in and around the small crater.

293 **Mineralogy and Geomorphology of the Cross Crater Region**

294 The mineralogy immediately outside of Cross crater is substantially different from that of
295 within (Figure 1d). No Al-phyllosilicates or sulfates are found; but in a survey of the
296 multispectral data within several Cross crater radii, there are at least a half dozen small (~10
297 km²) exposures of Fe/Mg-phyllosilicate-bearing materials. Fe/Mg-phyllosilicates are found in
298 several apparently sedimentary deposits as well as in small crater ejecta north of Cross crater.
299 These occurrences are associated with high thermal inertia materials (e.g. Figure 1c, 1d) yet have
300 a friable, eroded appearance (Figure 4b). To the south Fe/Mg-phyllosilicates are found together
301 with chlorides in a high thermal inertia deposit near 32°S, 157°W (see Osterloo et al., 2010;
302 Figure 13d in Ruesch et al., 2012].

303 Gridded MOLA DEM data of Cross crater paired with visible images show a ~4 km wide
304 valley that breaches the eastern crater rim, entering the Cross crater basin (Figure 7). No outflow
305 is apparent, and thus Cross crater is a closed basin. The valley enters the crater at an elevation of
306 1650 m—slightly above the 1550 m maximum height of the alunite and Al-phyllosilicate units—
307 from the topographic depression immediately east of the crater. The depression's present extent
308 is ~100 km², although its topography has been modified by a nearby impact crater to the east, so
309 the extent may have previously been greater. Interestingly, small knobs in the walls of the inlet
310 exhibit similar composition to the Cross crater sediments with Al-phyllosilicates and possibly

311 alunite. Four knobs in the valley wall have an absorption at 2.18-2.20 μm in materials that also
312 have a 1.9- μm absorption (Figure 7d). Analysis of HiRISE and CTX imagery shows that these
313 knobs are part of the walls of the valley, rather than ejecta or debris from the plateau above and
314 are not layered. They occur at an elevation of ~ 2000 m, i.e., ~ 400 -500 m above the highest
315 outcrops of alunite and Al-phyllsilicates minerals within layered Cross crater sediments.

316 **Discussion**

317 **The Cross crater mineral assemblage in a Martian context**

318 A number of intercrater depressions across Mars host chlorides or sulfates (Osterloo et
319 al., 2010; Gaillard et al., 2013; Ehlmann & Edwards, 2014). Carbonates have only been
320 identified in two potential lake basins (Ehlmann et al., 2009; Michalski et al., 2013). Only a few
321 dozen of the >200 potential closed-basin crater lakes on Mars exhibit evidence of hydrated
322 minerals in existing CRISM and OMEGA data (Goudge et al., 2015). In deep basins filled with
323 sediments (comparable in size and original depth to Cross crater), sulfates are typically the salt
324 present, associated with Fe/Mg-phyllsilicates, hematite, and silica (e.g., in Gale (Milliken et al.,
325 2010) and Terby craters (Ansan et al., 2011)). Meridiani Planum, explored by the Opportunity
326 rover, has jarosite within its spatially extensive sulfate-rich sediments (Klingelhofer et al., 2004;
327 Arvidson et al., 2006; Poulet et al., 2008). The Valles Marineris troughs and associated chaos
328 terrain also host sulfates, with some exposures including interbedded or overlying detrital
329 phyllsilicates or authigenic hydrated silicates (e.g., Gendrin et al., 2005; Murchie et al., 2009a;
330 Bishop et al., 2009; Lichtenberg et al., 2010; Roach et al., 2010; Thollot et al., 2012). Typical
331 Valles Marineris interior layered deposit mineralogy is of monohydrated Mg-sulfates
332 interbedded with or grading up-section into polyhydrated sulfates, both accompanied by
333 crystalline ferric oxides (Bibring et al., 2007; Murchie et al. 2009c). Some locales host evidence

334 for distinctly acidic conditions and sulfur-rich fluids. These include Gusev crater (Hurowitz &
335 McLennan, 2007; Morris et al., 2008; Wang et al., 2008); jarosite in some units at Northeastern
336 Syrtis Major (Ehlmann & Mustard, 2012) and Mawrth Vallis (Farrand et al., 2009; 2014); Valles
337 Marineris plateau deposits with jarosite and Fe(III)SO₄OH (Milliken et al., 2008; Weitz et al.,
338 2010); jarosite in Noctis Labyrinthus troughs (Thollot et al., 2012); szmolnokite and
339 Fe(III)SO₄OH low in the section in Aram chaos (Massé et al., 2008; Lichtenberg et al., 2010);
340 and chasma deposits whose spectra exhibit a “doublet” absorption that may be indicative of clays
341 that have been leached or mixed with jarosite (Roach et al., 2010; Weitz et al., 2011). Alunite has
342 not yet been detected in or around any of these regions.

343 Cross crater contains the first and, as of this writing, largest discovery of alunite deposits
344 on Mars. The outcrop with spectrally dominant alunite in the southwestern portion of the crater is
345 ~10 km x ~5 km in extent, and scattered smaller outcrops occur in several locations in Cross
346 crater, intermixed with kaolinite group minerals. On Mars, known occurrences of alunite are so
347 far restricted to three locations in the Terra Sirenum region: (i) Cross crater, (ii) nearby
348 Columbus crater, where it is found mixed with phyllosilicates in CRISM image, FRT00013EEF,
349 in a few hectometer-scale outcrops on the crater lower wall and floor, and (iii) a small light-
350 toned deposit within the intercrater plateau near Cross and Columbus (25.42°S, 161.17°W). As
351 described by Wray et al. (2011), Columbus crater has light-toned layered deposits similar in
352 morphology to some within Cross crater (Figure 6a, c) but with secondary minerals and
353 precipitates dominated by kaolinite and polyhydrated and monohydrated Ca/Mg/Fe-sulfates,
354 including gypsum and kieserite. Localized outcrops within Columbus contain Al-smectite clays,
355 Fe/Mg-phyllosilicates, jarosite, alunite, and crystalline ferric oxides. The interbedded kaolinite
356 and sulfates at Columbus are inferred to represent fluctuating lake levels within a deep, closed-

357 basin deep lake, fed by upwelling groundwaters (Wray et al., 2011). This mineral assemblage is,
358 however, distinct from that in Cross crater.

359 **Inferred Cross crater water chemistry**

360 At Cross crater, Al-rich and Si-rich phases—specifically, alunite, kaolinite group
361 phyllosilicates, and silica or montmorillonite—are the spectrally and spatially dominant
362 secondary minerals. Iron oxides and iron sulfates are also present but are less spatially
363 widespread at the surface. On Earth, this mineral assemblage is classically characteristic of acid
364 sulfate, advanced argillic alteration. As pH decreases, the solubility of Al^{3+} increases, making it a
365 mobile element and readily available for incorporation into precipitated secondary minerals. The
366 pH of waters implied by the presence of alunite is acidic and possibly as low as 2-3. Figure 8
367 presents mineral stability fields for select slices of the multi-dimensional geochemical parameter
368 space that illustrate key tradeoffs in predominance of alunite with other minerals. Under
369 conditions where Al^{3+} is enriched in fluids, kaolinite and alunite precipitate under similar
370 conditions but with alunite forming at lower pH and/or higher $a\text{SO}_4^{2-}$ than kaolinite (Figure 8a).
371 The formation of alunite also requires acid sulfate solutions that can mobilize K in addition to the
372 aluminum (Rye et al., 1992). Aluminum must be many times more concentrated than iron in
373 solution for alunite formation to be favored relative to jarosite formation (Figure 8b). Jarosite
374 precipitation also requires more oxidizing conditions than alunite precipitation (Figure 8c).
375 Alunite forms near the $\text{H}_2\text{S}-\text{SO}_2$ buffer at low $f\text{O}_2$, commonly in the near-subsurface (Rye et al.
376 1992; Stoffregen et al., 2000).

377 The co-existence of alunite, kaolinite group phyllosilicates, and silica or montmorillonite
378 may indicate temporally fluctuating pH conditions in waters whereby at low $a\text{SO}_4^{2-}$, kaolinite is
379 favored, whereas at lower pHs and/or higher sulfate contents, alunite preferentially precipitates

380 (Figure 8). Alternatively, a two-step formation process is possible. From preexisting Al-
381 phyllosilicates, alunite forms by their leaching with waters with sulfuric acid (e.g., Altheide et
382 al., 2010). In either case, Cross crater hosted distinctly sulfurous, acidic waters during at least
383 one part of its history. Determining the timing and environmental setting(s) of alunite and Al
384 phyllosilicate formation requires additional information, discussed below.

385 **Possible formation environments for large alunite deposits**

386 How could such a large-scale alunite-bearing deposit form on Mars in Cross crater? On
387 Earth, there are three main environmental settings of alunite precipitation: magmatic
388 hydrothermal systems, weathering of massive sulfide deposits (supergene alteration), and in
389 cratonic lakes fed by paleobrine. On Mars, there are at least four possibilities. For the first
390 possibility, in magmatic hydrothermal systems, H₂S or SO₂ gases interact with groundwaters,
391 which are then piped to the surface as brines or steam, often along structurally controlled faults
392 (e.g. John et al., 2008; Varekamp et al., 2009). For example, at Copahue volcano in the Andes,
393 argillaceous deposits along the crater lake and flanks of the volcano host alunite and kaolinite in
394 varying proportions, fed by groundwaters whose flow patterns are controlled by faults.
395 Accessory silica phases are interspersed as crusts and veins, and almost pure siliceous sinters
396 occur in zones with low pH. In this and other fumarolic systems, magmatic fluids contribute SO₂
397 that undergoes disproportionation as it cools to form highly acidic fluids, which boil at the
398 surface of a water table releasing H₂S- and H₂SO₄-rich steam that leaches overlying rocks
399 replacing them with alunite and silica (Rye et al., 1992). Lake margins deposits can also contain
400 jarosite, hematite, montmorillonite, gypsum, kaolinite, goethite and quartz; vent mouths have
401 sulfur and pyrite (Mas et al., 1996). The primary controls on mineralogy are pH, fO₂, and
402 presence of sulfurous species. Variability is driven by volcanic activity (the vigor of outgassing)

403 and seasonal fluxes, which dictate the relative proportion of meteoric waters to magmatic
404 groundwaters. The fluids containing H₂SO₄, SO₂, HF, and HCl acquire many rock-forming
405 elements from interaction with basaltic to basaltic-andesite protoliths but are not neutralized by
406 the interaction (Mas et al., 1996; Varekamp et al., 2009). Upon loss of S, either via decreased
407 production of volcanic steam or reaction with host rocks, sulfurous brines transition to alkaline
408 chloride fluids (Rye et al., 1992). On Mars, acid hydrothermal systems have been proposed for
409 sulfate and silica deposits observed by the Spirit Rover in Gusev crater (e.g., Squyres et al.,
410 2008; Wang et al., 2008) and sulfate deposits in Valles Marineris (e.g., Thollot et al., 2012).

411 A second possibility is the formation of acidic waters, and then alunite deposition, driven
412 by acidity produced during oxidative weathering of ferrous minerals, like sulfides and primary
413 mafic phases. Such processes typically result in the precipitation of Fe-rich minerals, including
414 ferrous and ferric sulfates as well as iron oxides and phyllosilicates (e.g., Fernandez-Remolar et
415 al., 2003; 2005; 2011; Swayze et al., 2000; 2008; Swayze et al., 2000). The oxidation and
416 hydrolysis of iron from sulfides releases H⁺ and is the source of acidity, which dictates the water
417 chemistry and drives subsequent reactions. In these settings, kaolinite and alunite can sometimes
418 be present when altered rocks are felsic or when leaching is intense. Evidence for large quantities
419 of buried sulfides have not been found on Mars, though sulfide weathering has been proposed to
420 explain sulfate deposits (Poulet et al., 2008; Dehouck et al., 2012), and a similar mechanism of
421 near-surface oxidation of Fe(II)-bearing sulfurous groundwaters has been proposed to generate
422 the acid conditions recorded at Meridiani Planum (Hurowitz et al., 2010).

423 A third possibility is that Cross crater was a paleolake, analogous to the acid saline lakes
424 of Western Australia (WA; e.g., Long et al., 1992; McArthur, 1991; Bowen & Benison, 2009;
425 Story et al., 2010). The WA lakes do not evolve from evapoconcentration of dilute inflow waters

426 but rather are fed by highly evolved, regionally acid-saline groundwaters. Lakes precipitate
427 halite, gypsum, hematite, kaolinite, and small amounts of basaluminite, bassanite, and alunite.
428 Shallow groundwaters in adjacent mudflats precipitate the same minerals, plus jarosite, which
429 forms syndepositionally as cements and displacive crystals (Benison et al., 2007; Story et al.,
430 2010; Bowen et al., 2012; Benison & Bowen, 2015). Alunite is an early diagenetic precipitate
431 within the pores of these deposits. Mixing in of meteoric waters, marine aerosols,
432 evapoconcentration, and mineral precipitation and dilution reactions control the chemistries of
433 individual lakes as well as their time variation. While several theories have been put forward for
434 understanding the origin of the acid saline waters, neither lithologic control (e.g., mafic vs. felsic
435 or presence/absence of massive sulfide), trapped ancient seawaters, or anthropogenic activities
436 can fully explain the observed chemical variability. The lack of natural buffers in a stable, highly
437 weathered craton, coupled with aridity to prevent dilution, may allow ancient acidic brines that
438 have evolved past the carbonate geochemical divide, consuming alkalinity, to acquire acidity
439 from small amounts of Fe, S, and rock weathering (Long et al., 1992; Bowen et al., 2012;
440 Benison& Bowen, 2015). Whether such multigeneration brines—or the equivalent of a
441 weathered craton—exist buried in the Mars subsurface is unknown, though production of
442 subsurface brines from dissolution of ancient salt deposits has been hypothesized (Zolotov and
443 Mironenko, 2014).

444 A fourth possibility may be distinctly Martian: highly acidified snows/rains. A
445 straightforward way to produce the requisite H₂SO₄-bearing solutions for alunite formation is via
446 disproportionation of SO₂ released by volcanism into the atmosphere, and subsequent aerosol
447 deposition (Bullock and Moore, 2007). Any waters – precipitation and/or snow/ice melt – would
448 become acidic by the incorporation of these hydrous sulfate species, present in the atmosphere

449 but also in the Martian soils where there is an imbalance with more anion species than cations
450 (Settle, 1979). These acidified waters could episodically form ponds in Cross crater and in
451 surrounding depressions.

452 **Environment of Alunite Formation in Cross Crater**

453 Geologic associations of minerals present can be used to discriminate between the four
454 possibilities above to establish environmental conditions for the formation of Cross crater's
455 deposits. Most open- and closed-basin lakes on Mars with evidence for secondary minerals
456 exhibit phyllosilicates within the basins that are spectrally identical to materials in the nearby
457 watershed, suggesting transport and deposition may be responsible for the current distribution of
458 these minerals, rather than in situ precipitation (Goudge et al., 2012a; 2015). In Cross crater,
459 however, phyllosilicate mineralization likely occurred in situ because kaolin-bearing sediments
460 within the basin differ markedly from Fe/Mg-phyllosilicates present in plains outside the crater.
461 The existence of extensive kaolinite group minerals and alunite within the basin points to a
462 special geologic process or a peculiar sediment or water chemistry uniquely confined to the
463 Cross crater basin and, perhaps, nearby Columbus crater and the plateaus between.

464 The acid aerosol mechanism may contribute to explaining regional Al-phyllosilicate
465 formation by regional intensification of weathering (e.g., Wray et al., 2011; Ehlmann &
466 Edwards, 2014; Carter et al., 2015), but it does not explain the particular localized concentration
467 of alunite in Cross crater. Iron sulfide dissolution or iron oxidation mechanisms likely provide a
468 source of acidity elsewhere on Mars, but do not alone explain alunite formation here because of
469 the paucity of Fe-bearing alteration phases, which are typical products of this process and are
470 detected with remote sensing at many other Martian localities. Mars is mostly comprised of

471 basaltic rocks, and the paucity of Fe/Mg/Ca secondary minerals and dominance of aluminum
472 minerals in Cross crater is atypical.

473 Mineralized, layered sediments along a contour roughly coincident with the mouth of an
474 inlet valley suggest the past presence of a closed basin lake in Cross crater. Lake levels at 1500
475 m (maximum elevation of layered sediments with Al-phyllsilicates) or 1650 m (inflow channel
476 elevation) would have resulted in lake volumes of approximately 1500 km³ or 1900 km³,
477 respectively, comparable to the volume of terrestrial Lake Ontario (1700 km³). Alternatively,
478 successive episodic periods of sedimentation and fill may have produced the observed sediments
479 via a series of shallow playa lakes or via weathering of airfall deposits. Acquisition of additional
480 HiRISE stereo pairs – only two on the southern wall exist to date – would facilitate the search for
481 shoreline terraces and correlation of bed levels as indicators of lake level.

482 A key question is the source and nature of any waters feeding the basin. Although the
483 depression in which the Cross crater inflow channel is sourced does not constitute a well-
484 bounded basin, the entire region lies just east of the Eridania drainage network (Irwin et al.,
485 2004), thought to be fed at least partially by groundwater (Fassett and Head, 2008). Moreover,
486 Cross crater is located south of the Mangala Vallis outflow, a unique valley system on Mars,
487 where a large outflow is sourced by a small fracture. An extensive groundwater system has been
488 suggested for the eastern flank of Tharsis (Ghatan et al., 2005 and references therein) and may
489 provide a source of waters for a paleo-Cross crater lake. Waters may have acquired acidity by
490 exchange with sulfurous compounds in meteoric waters or via subsurface exchange with
491 hydrothermal fluids, paleobrines, or iron sulfides. As modeled by Andrews-Hanna et al. (2010)
492 and discussed in Wray et al. (2011), Cross and Columbus craters are expected to be sites of
493 groundwater upwelling forming closed basin lakes and evaporate deposits.

494 However, that the most spectrally dominant alunite is geographically restricted to the
495 southwestern portion of the crater in spite of exposure of sedimentary materials with Al
496 phyllosilicates across the whole crater argues for a process that concentrates the alunite
497 formation in that area. In a ~800-m crater-wide deep lake, one would not expect highly localized
498 chemistry except in special circumstances. One possibility is the presence of localized, perhaps
499 fault-controlled, conduits for sulfurous groundwaters to reach the surface that are geographically
500 restricted to the southwest and result in fumarolic or hydrothermal spring deposits. A second
501 possibility is the existence of multiple shallow lakes within the basin, one of which was in the
502 southwest corner. Because the alunite is topographically higher than the silica-rich and kaolin-
503 rich deposits, the former possibility may be more likely than the latter. Additionally, the alunite
504 units are massive, rather than discretely layered. This may reflect their formation in the
505 subsurface as upwelling H₂S- or SO₂-bearing steam or fluids cooled, generating H₂SO₄ through
506 disproportionation. Oxidation upon contacting the Mars atmosphere or fluids in communication
507 with the Mars atmosphere would still further enhance sulfur speciation to SO₄²⁺. Finally, a third
508 inter crater plateau alunite-bearing site was found for which a non-lake-mediated formation
509 process is favored. There, alunite also occurs mixed with kaolinite group minerals within light-
510 toned deposits underlying an eroded cap-rock, but these are not in a topographic low.

511 Thus, localized conduits for escape of steam or waters in contact with magmatic sources
512 at depth is our favored hypothesis for the Cross crater alunite deposits. Numerous basins on Mars
513 show evidence of volcanic resurfacing (Goudge et al., 2012b), and Cross crater is located on the
514 western margin of the Tharsis system (Figure 1), a possible location of dike formation and a
515 location with numerous tectonic fractures, facilitating communication with the subsurface
516 (Anderson et al., 2001). The mineralogy of the Cross crater deposits with alunite, Al-

517 phyllosilicates, silica and scattered Fe oxides and Fe sulfates is similar to that observed in some
518 terrestrial magmatic systems. A flux of steam or waters from a magmatic hydrothermal system
519 into a basin that episodically may have hosted shallow lakes appears to fit the overall deposit
520 morphology and observed mineral assemblages.

521 In terrestrial settings, large alunite deposits are more typically associated with acid
522 alteration of either felsic rocks (e.g., Bigham and Nordstrom, 2000) or preexisting Al
523 phyllosilicates (e.g., Altheide et al., 2010). In basaltic hydrothermal alteration systems, alunite is
524 often a minor phase (Swayze et al., 2002; Guinness et al., 2007; Hynek et al., 2013; Marucci et
525 al., 2013). However, large-scale alteration to alunite and kaolinite assemblages mappable by
526 VSWIR imaging spectroscopy is also occasionally observed, driven in part by the duration of
527 magmatic activity at a particular locale (e.g. Berger et al., 2003; Swayze et al., 2014)
528 Furthermore, the crystallinity of protolith materials can strongly influence weathering products.
529 Weathering experiments by Tosca et al (2004) showed formation of Al-sulfates from basaltic
530 glass but not crystalline basalt of identical chemical composition. This is because Al in a glassy
531 material is released into solution during congruent dissolution whereas Al is typically retained in
532 rock in a dissolution process involving crystalline feldspar. Thus, (a) high throughput of acidic
533 waters, (b) poorly crystalline materials, and/or (c) more felsic precursors may – separately or in
534 combination – be responsible for the unique Cross crater alunite.

535 Future work might include more detailed geochemical modeling of a variety of potential
536 fluid and sediment compositions to further constrain the geochemical setting. Multistep
537 formation scenarios could be modeled with reaction-transport models and compared to the
538 composition and distribution of observed deposit mineralogy. A key question is the fate of
539 leached Fe, Ca and Mg, thus explaining the differences between Cross crater and nearby

540 Columbus crater with its polyhydrated sulfate, gypsum, and kieserite deposits. These salts are
541 either absent in Cross crater (precipitation in the subsurface, brine transport out of Cross crater
542 through highly permeable rocks?) or concealed in the basin center by the caprock. Furthermore,
543 questions of the potential extent, depth, and longevity of a Cross crater lake may be resolvable
544 with additional high spatial resolution mineralogic and topographic data over unimaged regions
545 in Cross crater. A key question whether any paleolakes and magmatic hydrothermal systems
546 facilitating alunite formation were contemporaneous.

547 **Implications**

548 Cross crater hosts the largest-scale alunite deposit discovered to date on Mars. It is
549 associated with basin-ringing, layered kaolin-bearing sediments as well as hydrated silica or
550 montmorillonite in polygonally-fractured sediments within local topographic lows. Evidence for
551 low pH aqueous activity on Mars has been previously provided by ferric sulfates, including
552 jarosite, formed at $\text{pH} < 4$. The discovery of alunite adds to the continuum of low pH Martian
553 environments with a distinctly different local geochemistry resulting in relatively iron- (and
554 magnesium- and calcium-) poor assemblages of phyllosilicates and sulfates. Along with the
555 smaller deposits in nearby Columbus crater and on the plateau in between, Cross crater's alunite
556 deposits are indicative of regional conditions. Prevalent alunite and accompanying Al
557 phyllosilicates require acidity and (1) locally high volumes of sulfurous groundwaters with H_2S
558 or SO_2 and high water throughput during alteration; (2) atypically glassy and/or felsic basin-
559 filling materials, more susceptible to dissolution and mobilization of aluminum; or a combination
560 of these. Cross crater, with its advanced argillic alteration, including alunite precipitates, thus
561 represents a new type of ancient Martian aqueous environment.

References

- 583
584
- 585 Altheide, T.S., Chevrier, V.F., and Noe Dobrea, E. (2010) Mineralogical characterization of acid
586 weathered phyllosilicates with implications for secondary martian deposits. *Geochimica*
587 *et Cosmochimica Acta* 74, 6232–6248
- 588 Anderson, R. C., Dohm, J. M., Golombek, M. P., Haldemann, A. F. C., Franklin, B. J., Tanaka,
589 K. L., Lias, J., and Peer B. (2001) Primary centers and secondary concentrations of
590 tectonic activity through time in the western hemisphere of Mars, *Journal of Geophysical*
591 *Research*, 106, 20,563–20,585, doi:10.1029/2000JE001278.
- 592 Andrews-Hanna, J. C., Zuber, M. T., Arvidson, R. E. and Wiseman, S. M. (2010) Early Mars
593 hydrology: Meridiani playa deposits and the sedimentary record of Arabia Terra, *Journal*
594 *of Geophysical Research*, 115, E06002, doi:10.1029/2009JE003485.
- 595 Ansan, V., et al. (2011) Stratigraphy, mineralogy, and origin of layered deposits inside Terby
596 crater, Mars, *Icarus*, 211, 273–304, doi:10.1016/j.icarus.2010.09.011.
- 597 Arvidson, R. E., et al. (2006) Nature and origin of the hematite-bearing plains of Terra Meridiani
598 based on analyses of orbital and Mars Exploration rover data sets, *Journal of Geophysical*
599 *Research*, 111, E12S08, doi:10.1029/2006JE002728.
- 600 Benison, K.C., Bowen, B.B., Oboh-Ikuenobe, F.E., Jagniecki, E.A., LaClair, D.A., Story, S.L.,
601 Mormile, M.R., and Hong, B. (2007) Sedimentary processes and products of ephemeral
602 acid saline lakes in southern Western Australia *Journal of Sedimentary Research* 77,
603 366–388.

604 Benison, K.C., and Bowen, B.B. (2015) The evolution of end-member continental waters: The
605 origin of acidity in southern Western Australia. *GSA Today*, 25(6), 4-10.

606 Berger, B.R., King, T.V.V., Morath, L.C., and Phillips, J.D. (2003) Utility of high-altitude
607 infrared spectral data in mineral exploration: Application to northern Patagonia
608 Mountains, Arizona. *Economic Geology*, 98, 1003-1018.

609 Bibring, J.-P., et al. (2005) Mars surface diversity as revealed by the OMEGA/Mars Express
610 observations, *Science*, 307, 1576 – 1581, doi:10.1126/science.1108806.

611 Bibring, J.-P., et al. (2006) Global mineralogical and aqueous Mars history derived from
612 OMEGA/Mars Express data, *Science*, 312, 400 – 404, doi:10.1126/science.1122659.

613 Bibring, J.-P., et al. (2007) Coupled ferric oxides and sulfates on the Martian surface, *Science*,
614 317, 1206 – 1210, doi:10.1126/science. 1144174.

615 Bishop, J., Madejova, J., Komadel, P., and Froschl, H. (2002a), The influence of structural Fe,
616 Al, and Mg on the infrared OH bands in spectra of dioctahedral smectites, *Clay Minerals*,
617 37, 607 – 616, doi:10.1180/0009855023740063.

618 Bishop, J. L., Murad, E., and Dyar, M. D. (2002b) The influence of octahedral and tetrahedral
619 cation substitution on the structure of smectites and serpentines as observed through
620 infrared spectroscopy, *Clay Minerals.*, 37, 617– 628, doi:10.1180/0009855023740064.

621 Bishop, J.L. and Murad, E. (2005) The visible and infrared spectral properties of jarosite and
622 alunite. *American Mineralogist*, 90, 1100–1107.

623 Bishop, J. L., Lane, M. D., Dyar, M. D., and Brown, A. J. (2008) Reflectance and emission
624 spectroscopy of four groups of phyllosilicates: Smectites, kaolinite-serpentines, chlorites,
625 and micas, *Clay Minerals*, 43, 35– 54, doi:10.1180/claymin.2008.043.1.03.

626 Bishop, J. L., et al. (2009) Mineralogy of Juventae Chasma: Sulfates in the light-toned mounds,
627 mafic minerals in the bedrock, and hydrated silica and hydroxylated ferric sulfate on the
628 plateau, *Journal of Geophysical Research*, 114, E00D09, doi:10.1029/2009JE003352.

629 Bowen, B. B., and Benison, K. C. (2009) Geochemical characteristics of naturally acid and
630 alkaline saline lakes in southern Western Australia, *Applied Geochemistry*, 24, 268–284,
631 doi:10.1016/j.apgeochem.2008.11.013.

632 Bowen, B.B., Benison, K.C., and Story, S. (2012) Early diagenesis by modern acid brines in
633 Western Australia and implications for the history of sedimentary modification on Mars.
634 Society for Sedimentary Geology Special Publication, *Mars Sedimentology*, eds.,
635 Grotzinger, J. and Milliken R., SEPM Special Publication No. 102, p. 229-252.

636 Bullock, M.A., and Moore, J.M. (2007) Atmospheric conditions on early Mars and the missing
637 layered carbonates: *Geophysical Research Letters*, v. 34, L19201,
638 doi:10.1029/2007GL030688.

639 Carr, M.H., 1996. *Water on Mars*. Oxford University Press. 248 pp.

640 Carter, J., Poulet, F., Bibring, J.-P., Mangold, N., and Murchie, S. (2013) Hydrous minerals on
641 Mars as seen by the CRISM and OMEGA imaging spectrometers: Updated global view,
642 *Journal of Geophysical Research Planets*, 118, doi: 10.1029/2012JE004145.

643 Carter, J., Loizeau, D., Mangold, N., Poulet, F., and Bibring, J.-P. (2015) Widespread surface
644 weathering on early Mars: A case for a warmer and wetter climate. *Icarus* 248: 373-382.

645 Christensen, P. R., et al. (2001) Mars Global Surveyor Thermal Emission Spectrometer
646 experiment: Investigation description and surface science results, *Journal of Geophysical*
647 *Research*, 106(E10), 23,823–23,871, doi:10.1029/2000JE001370.

648 Christensen, P. R., et al. (2004) The Thermal Emission Imaging System (THEMIS) for the Mars
649 2001 Odyssey mission, *Space Science Reviews*, 110, 85–130,
650 doi:10.1023/B:SPAC.0000021008.16305.94.

651 Clark, R. N., King, T. V. V., Klejwa, M., Swayze, G. A., and Vergo, N. (1990) High spectral
652 resolution reflectance spectroscopy of minerals, *Journal of Geophysical Research*, 95,
653 12,653–12,680, doi:10.1029/JB095iB08p12653.

654 Clark, R.N., Swayze, G.A., Livo, K.E., Kokaly, R.F., Sutley, S.J., Dalton, J.B., McDougal,
655 R.R., and Gent, C.A. (2003) Imaging spectroscopy: Earth and planetary remote sensing
656 with the USGS Tetracorder and Expert Systems. *Journal of Geophysical Research*, 108,
657 no. E12, 5131, doi:10.1029/2002JE001847, 44 p.

658 Clark, R.N., Swayze, G.A., Wise, R., Livo, E., Hoefen, T., Kokaly, R., and Sutley, S.J. (2007)
659 USGS digital spectral library splib06a: U.S. Geological Survey, Data Series 231,
660 <http://speclab.cr.usgs.gov/spectral-lib.html>

661 Dehouck, E., Chevrier, V., Gaudin, A., Mangold, N., Mathe, P.-E., and Rochette, P. (2012)
662 Evaluating the role of sulfide-weathering in the formation of sulfates or carbonates on
663 Mars. *Geochimica et Cosmochimica Acta* 90, 47–63.

664 Edwards, C. S., K. J. Nowicki, P. R. Christensen, J. Hill, N. Gorelick, and K. Murray (2011)
665 Mosaicking of global planetary image datasets: 1. Techniques and data processing for
666 Thermal Emission Imaging System (THEMIS) multi-spectral data, *Journal of*
667 *Geophysical Research*, 116, E10008, doi:10.1029/2010JE003755.

668 Ehlmann, B.L. and Edwards, C.S., (2014) Mineralogy of the Martian Surface. *Annual Reviews*
669 *of Earth and Planetary Sciences*, 42; doi: 10.1146/annurev-earth-060313-055024.

670 Ehlmann, B. L., and J. F. Mustard (2012) An in-situ record of major environmental transitions on
671 early Mars at Northeast Syrtis Major, *Geophysical Research Letters*, 39, L11202,
672 doi:10.1029/2012GL051594.

673 Ehlmann, B. L., et al. (2008) Orbital identification of carbonate-bearing rocks on Mars, *Science*,
674 322, 1828– 1832, doi:10.1126/science.1164759.

675 Ehlmann, B. L., et al. (2009) Identification of hydrated silicate minerals on Mars using MRO-
676 CRISM: Geologic context near Nili Fossae and implications for aqueous alteration,
677 *Journal of Geophysical Research*, 114, E00D08, doi:10.1029/2009JE003339.

678 Farrand, W.H., Glotch, T.D., Rice, J.W. Jr., Hurowitz, J.A., and Swayze, G.A. (2009) Discovery
679 of jarosite within the Mawrth Vallis region of Mars: Implications for the geologic history
680 of the region. *Icarus*, 204, 478–488.

681 Farrand, W.H., Glotch, T.D., and Horgan, B. (2014) Detection of copiapite in the northern
682 Mawrth Vallis region of Mars: Evidence of acid sulfate alteration. *Icarus* 241, 346–357.

683 Fassett, C.I. and Head, J.W., III (2008) Valley network-fed, open-basin lakes on Mars:
684 Distribution and implications for Noachian surface and subsurface hydrology. *Icarus*,
685 198, 37-56.

686 Ferguson et al. (2006) High-resolution thermal inertia derived from the Thermal Emission
687 Imaging System (THEMIS): Thermal model and applications, *Journal of Geophysical*
688 *Research*, 111(E12004), doi:10.1029/2006JE002735.

689 Fernández-Remolar, D., Rodríguez, N., Gómez, F., and Amils, R. (2003) The geological record
690 of an acidic environment driven by iron hydrochemistry: The Tinto River system. *Journal*
691 *of Geophysical Research* 108 (E7). doi:10.1029/2002JE001918.

692 Fernández-Remolar, D.C., Morris, R.V., Gruener, J.E., Amils, R., and Knoll, A.H. (2005) The
693 Río Tinto basin, Spain: Mineralogy, sedimentary geobiology, and implications for
694 interpretation of outcrop rocks at Meridiani Planum, Mars. *Earth and Planetary Science*
695 *Letters* 240 (1), 149–167.

696 Fernández-Remolar, D. C., Prieto-Ballesteros, O., Gómez-Ortíz, D., Fernández-Sampedro, M.,
697 Sarrazin, P., Gailhanou, M., and Amils, R. (2011) Río Tinto sedimentary mineral
698 assemblages: A terrestrial perspective that suggests some formation pathways of
699 phyllosilicates on Mars, *Icarus*, 211 ,114 – 138, doi:10.1016/j.icarus.2010.09.008.

700 Gaillard, F., Michalski, J., Berger, G., McLennan, S.M., and Scaillet, B. (2013) Geochemical
701 reservoirs and timing of sulfur cycling. *Space Science Reviews* 174, 251-300.

702 Gendrin, A., et al. (2005) Sulfates in Martian layered terrains: The OMEGA/Mars Express view,
703 *Science*, 307, 1587–1591, doi:10.1126/science.1109087.

704 Ghatan, G.J., Head, J.W. III, and Wilson, L. (2005). Mangala Valles, Mars: Assessment of early
705 stages of flooding and downstream flood evolution. *Earth, Moon, and Planets*, 96, 1-57.

706 Gondet, B., Bibring, J.-P., Langevin, Y., Poulet, F., and Gendrin, A. (2006) First detection of Al-
707 rich phyllosilicate on Mars from OMEGA-Mex. *Geophysical Research Abstracts*, 8,
708 03691, European Geosciences Union, 1607-7962/gra/EGU06-A-03691

709 Goudge, T.A. Head, J.W., Mustard, J.F., and C. I. Fassett (2012a) An analysis of open-basin lake
710 deposits on Mars: Evidence for the nature of associated lacustrine deposits and post-
711 lacustrine modification processes. *Icarus* 219, 211–229.

712 Goudge, T. A., Mustard, J.F., Head, J. W. and Fassett, C. I. (2012b) Constraints on the history of
713 open-basin lakes on Mars from the composition and timing of volcanic resurfacing,
714 *Journal of Geophysical Research*, 117, E00J21, doi:10.1029/2012JE004115

715 Goudge, T.A., Aureli, K.L., Head, J.W., Fassett, C.I., and Mustard, J.F. (2015) Classification and
716 analysis of candidate impact crater-hosted closed-basin lakes on Mars. *Icarus* 260, 346–
717 367

718 Guinness, E. A., Arvidson, R. E., Jolliff, B. L., Seelos, K. D., Seelos, F. P., Ming, D. W., Morris,
719 R. V., and Graff, T. G. (2007) Hyperspectral reflectance mapping of cinder cones at the
720 summit of Mauna Kea and implications for equivalent observations on Mars, *Journal of*
721 *Geophysical Research*, 112, E08S11, doi:10.1029/2006JE002822.

722 Hunt, G.R., Salisbury, J.W., and Lenhoff, C.J. (1971) Visible and near-infrared spectra of
723 minerals and rocks: IV. Sulphides and sulphates. *Modern Geology*, 3, 1-14.

724 Hunt, G. R. (1977) Spectral signatures of particulate minerals, in the visible and near-infrared,
725 Geophysics, 42, 501 – 513.

726 Hurowitz, J. A. and McLennan, S. M. (2007) A 3.5 Ga record of waterlimited, acidic weathering
727 conditions on Mars, Earth and Planetary Science Letters, 260, 432–443,
728 doi:10.1016/j.epsl.2007.05.043.

729 Hurowitz, J.A., Fischer, W.W., Tosca, N.J., and Milliken, R.E. (2010) Origin of acidic surface
730 waters and the evolution of atmospheric chemistry on early Mars. Nature Geoscience, 3,
731 323 – 326.

732 Hynek, B. M., McCollom, T. M., Marcucci, E. C., Brugman, K. and Rogers, K. L. (2013)
733 Assessment of environmental controls on acid-sulfate alteration at active volcanoes in
734 Nicaragua: Applications to relic hydrothermal systems on Mars, Journal of Geophysical
735 Research Planets, 118, 2083–2104, doi:10.1002/jgre.20140.

736 Irwin, R. P., III, Howard, A. D. and Maxwell, T. A. (2004) Geomorphology of Ma’adim Vallis,
737 Mars, and associated paleolake basins, Journal of Geophysical Research, 109, E12009,
738 doi:10.1029/2004JE002287.

739 John, D.A., Sisson, T.W., Breit, G.N., Rye, R.O., and Vallance, J.W. (2008) Characteristics,
740 extent and origin of hydrothermal alteration at Mount Rainier Volcano, Cascades Arc,
741 USA: Implications for debris-flow hazards and mineral deposits. Journal of Volcanology
742 and Geothermal Research, 175, 289–314.

743 Klingelhöfer, G., et al. (2004) Jarosite and hematite at Meridiani Planum from Opportunity’s
744 Mössbauer spectrometer, Science, 306(5702), 1740–1745, doi:10.1126/science.1104653

745 Lichtenberg, K. A., et al. (2010) Stratigraphy of hydrated sulfates in the sedimentary deposits of
746 Aram Chaos, Mars, *Journal of Geophysical Research*, 115, E00D17,
747 doi:10.1029/2009JE003353.

748 Long, D.T., Fegan, N.E., McKee, J.D., Lyons, W.B., Hines, M.E., and Macumber, P.G. (1992)
749 Formation of alunite, jarosite and hydrous iron oxides in a hypersaline system: Lake
750 Tyrell, Victoria, Australia, *Chemical Geology* 96, 183– 202.

751 Malin M. C., et al. (2007), Context Camera Investigation on board the Mars Reconnaissance
752 Orbiter: *Journal of Geophysical Research*, 112, E05S04, doi:10.1029/2006JE002808.

753 Marcucci, E.C., Hynek, B.M., Kierein-Young, K.S., and Rogers, K.L. (2013) Visible-near
754 infrared reflectance spectroscopy of volcanic acid-sulfate alteration in Nicaragua: Analogs
755 for early Mars. *Journal of Geophysical Research*, 118, 2213–2233,
756 DOI:10.1002/jgre.20159.

757 Mas, G.R., Mas, L.C., and Bengochea, L. (1996) Hydrothermal surface alteration in the Copahue
758 geothermal field (Argentina). *Proceedings, 21st workshop on Geothermal Reservoir
759 Engineering, Stanford University, Palo Alto California, January 22-24, 1996, SGP-TR-
760 151.*

761 Massé, M., Le Mouelic, S., Bourgeois, O., Combe, J.-P., Le Deit, L., Sotin, C., Bibring, J.-P.,
762 Gondet, B., and Langevin, Y. (2008) Mineralogical composition, structure, morphology,
763 and geological history of Aram Chaos crater fill on Mars derived from OMEGA Mars
764 Express data, *Journal of Geophysical Research*, 113, E12006,
765 doi:10.1029/2008JE003131.

766 McArthur, J. M., Turner, J. V., Lyons, W. B., Osborn, A. O. and Thirwall, M. F. (1991)
767 Hydrochemistry on the Yilgarn Block, Western Australia: Ferrolysis and mineralisation
768 in acidic brines, *Geochimica Cosmochimica Acta*, 55, 1273–1288, doi:10.1016/0016-
769 7037(91)90306-P.

770 McCollom, T.M., Ehlmann, B.L., Wang, A., Hynek, B.M., Moskowitz, B., and Berquo, T.S.
771 (2014) Detection of iron substitution in natroalunite-natrojarosite solid solutions and
772 potential implications for Mars, *American Mineralogist*, 99, 948-964, doi:
773 10.2138/am.2014.4617, 2014.

774 McEwen A. S., et al. (2007) Mars Reconnaissance Orbiter's High Resolution Imaging Science
775 Experiment (HiRISE), *Journal of Geophysical Research*, 112, E05S02,
776 doi:10.1029/2005JE002605.

777 Michalski, J. R., Cuadros, J., Niles, P.B., Parnell, J., Rogers, A.D., and Wright, S.P. (2013)
778 Groundwater activity on Mars and implications for a deep biosphere. *Nature Geoscience*,
779 6, 133-138.

780 Milliken, R. E., et al. (2008) Opaline silica in young deposits on Mars, *Geology*, 36, 847– 850,
781 doi:10.1130/G24967A.1.

782 Milliken, R. E., Fischer, W. W. and Hurowitz, J. A. (2009) Missing salts on early Mars,
783 *Geophysical Research Letters*, 36, L11202, doi:10.1029/2009GL038558.

784 Milliken, R. E., Grotzinger, J. P., and Thomson, B. J. (2010) Paleoclimate of Mars as captured
785 by the stratigraphic record in Gale Crater, *Geophysical Research Letters*, 37, L04201,
786 doi:10.1029/2009GL041870.

787 Morris, R. V., et al. (2008) Iron mineralogy and aqueous alteration from Husband Hill through
788 Home Plate at Gusev Crater, Mars: Results from the Mössbauer instrument on the Spirit
789 Mars Exploration Rover, *Journal of Geophysical Research*, 113, E12S42,
790 doi:10.1029/2008JE003201.

791 Murchie, S. L., et al. (2007) Compact Reconnaissance Imaging Spectrometer for Mars (CRISM)
792 on Mars Reconnaissance Orbiter (MRO), *Journal of Geophysical Research*, 112, E05S03,
793 doi:10.1029/2006JE002682.

794 Murchie, S. L., et al. (2009a) A synthesis of Martian aqueous mineralogy after one Mars year of
795 observations from the Mars Reconnaissance Orbiter, *Journal of Geophysical Research*,
796 114, E00D06, doi:10.1029/2009JE003342.

797 Murchie, S. L., et al. (2009b) Compact Reconnaissance Imaging Spectrometer investigation and
798 data set from the Mars Reconnaissance Orbiter's primary science phase, *Journal of*
799 *Geophysical Research*, 114, E00D07, doi:10.1029/2009JE003344.

800 Murchie, S., et al. (2009c) Evidence for the origin of layered deposits in Candor Chasma, Mars,
801 from mineral composition and hydrologic modeling, *Journal of Geophysical Research*,
802 114, E00D05, doi:10.1029/2009JE003343.

803 Mustard, J. F., et al. (2008) Hydrated silicate minerals on Mars observed by the CRISM
804 instrument on MRO, *Nature*, 454, 305– 309, doi:10.1038/nature07097.

805 Osterloo, M. M., Hamilton, V. E., Bandfield, J. L., Glotch, T. D., Baldrige, A. M.,
806 Christensen, P. R., Tornabene, L. L., and Anderson, F. S. (2008) Chloride-bearing

807 materials in the southern highlands of Mars, *Science*, 319, 1651–1654,
808 doi:10.1126/science.1150690.

809 Osterloo, M. M., Anderson, F. S., Hamilton, V. E., and Hynek, B. M. (2010) Geologic context of
810 proposed chloride-bearing materials on Mars, *Journal of Geophysical Research*, 115,
811 E10012, doi:10.1029/2010JE003613.

812 Pelkey, S. M., et al. (2007) CRISM multispectral summary products: Parameterizing mineral
813 diversity on Mars from reflectance, *Journal of Geophysical Research*, 112, E08S14,
814 doi:10.1029/2006JE002831.

815 Poulet, F., J.-P. Bibring, J. F. Mustard, A. Gendrin, N. Mangold, Y. Langevin, R. E. Arvidson, B.
816 Gondet, and C. Gomez (2005) Phyllosilicates on Mars and implications for early Martian
817 climage change, *Nature*, 438, 623–627, doi:10.1038/nature04274.

818 Poulet, F., Arvidson, R. E., Gomez, C., Morris, R. V., Bibring, J.-P., Langevin, Y., Gondet, B.,
819 and Griffes, J. (2008) Mineralogy of Terra Meridiani and western Arabia Terra from
820 OMEGA/MEx and implications for their formation, *Icarus*, 195, 106–130,
821 doi:10.1016/j.icarus.2007.11.031.

822 Ruesch, O., Poulet, F., Vincendon, M., Bibring, J.-P., Carter, J., Erkeling, G., Gondet, B.,
823 Hiesinger, H., Ody, A., and Reiss, D. (2012) Compositional investigation of the proposed
824 chloride-bearing materials on Mars using near-infrared orbital data from OMEGA/MEx,
825 *Journal of Geophysical Research*, 117, E00J13, doi:10.1029/2012JE004108.

826 Roach, L. H., et al. (2010) Hydrated mineral stratigraphy of Ius Chasma, Valles Marineris, *Icarus*,
827 206(1), 253–268, doi:10.1016/j.icarus.2009.09.003.

828 Rye, R.O., Bethke, P.M., and Wasserman, M.D. (1992) The stable isotope geochemistry of acid
829 sulphate alteration: *Economic Geology*, v. 87, no. 2, p. 225-262.

830 Settle, M. (1979) Formation and deposition of volcanic sulfate aerosols on Mars. *Journal of*
831 *Geophysical Research*, 84(B14), 8343-8354.

832 Smith, D.E. et al. (2001) Mars Orbiter Laser Altimeter: Experiment summary after the first year
833 of global mapping of Mars. *Journal of Geophysical Research Planets*, 106(E10), 23,689-
834 23,722.

835 Squyres, S. W., et al. (2004a) The Spirit Rover's Athena Science Investigation at Gusev Crater,
836 Mars, *Science*, 305, 794–799, doi:10.1126/science.3050794

837 Squyres, S. W., et al. (2004b) In situ evidence for an ancient aqueous environment at Meridiani
838 Planum, Mars, *Science*, 306(5702), 1709 – 1714, doi:10.1126/science.1104559.

839 Squyres, S. W., et al. (2008) Detection of silica-rich deposits on Mars, *Science*, 320, 1063–1067,
840 doi:10.1126/science.1155429.

841 Stoffregen, R.E., Alpers, C.N., and Jambor, J.L. (2000) Alunite-jarosite crystallography,
842 thermodynamics, and geochemistry. In: Alpers, C.N., Jambor, J.L., Nordstrom, D.K.
843 (Eds.), *Sulfate Minerals: Crystallography, Geochemistry, and Environmental*
844 *Significance, Reviews in Mineralogy*, vol. 40. Mineral. Soc. Am., Washington, DC, pp.
845 453–479.

846 Story, S., Bowen, B. B., Benison, K. C. and Schulze, D. G. (2010) Authigenic phyllosilicates in
847 modern acid saline lake sediments and implications for Mars, *Journal of Geophysical*
848 *Research*, 115 , E12012, doi:10.1029/2010JE003687

849 Swayze, G. A., (1997) The hydrothermal and structural history of the Cuprite mining district,
850 southwestern Nevada: An integrated geological and geophysical approach, Ph.D. thesis,
851 399 pp., Univ. of Colorado, Boulder, Colo.

852 Swayze, G.A., et al. (2000) Using imaging spectroscopy to map acidic mine waste.
853 Environmental Science and Technology, v. 34, no. 1, p. 47-54.

854 Swayze, G.A., Clark, R.N., Sutley, S.J., Gent, C.A., Rockwell, B.W., Blaney, D.L., Post, J.L.,
855 and Farm, B.P. (2002) Mineral mapping Mauna Kea and Mauna Loa Shield Volcanos on
856 Hawaii using AVIRIS data and the USGS Tetracorder spectral identification system:
857 Lessons applicable to the search for relict Martian hydrothermal systems. Proceedings of
858 the 11th JPL Airborne Earth Science Workshop, R.O. Green (ed.), Jet Propulsion
859 Laboratory Publication 03-4, p. 373-387.

860 Swayze, G.A., Desborough, G.A., Clark, R.N., Rye, R.O., Stoffregen, R.E., Smith, K.S., and
861 Lowers, H.A. (2006) Detection of jarosite and alunite with hyperspectral imaging:
862 prospects for determining their origin on Mars using orbital sensors in Martian Sulfates
863 As Recorders of Atmospheric-Fluid-Rock Interactions, October 22–24, 2006, Houston,
864 TX, abstract 7072.

865 Swayze, G. A., et al. (2007) Spectral evidence for hydrated volcanic and/or impact glass on Mars
866 with MRO CRISM, in Seventh International Conference on Mars, July 9 – 13, 2007,
867 Pasadena CA, abstract 1353.

868 Swayze, G. A., et al. (2008) Discovery of the acid-sulfate mineral alunite in Terra Sirenum,
869 Mars, using MRO CRISM: Possible evidence for acid-saline lacustrine deposits? Eos

870 Transactions of the American Geophysical Union 89(53), Fall Meeting Supplement,
871 abstract P44A-04.

872 Swayze, G.A., Clark, R.N., Goetz, F.H., Livo, K.E., Breit, G.N., Kruse, F.A., Sutley, S.J., Snee,
873 L.W., Lowers, H.A., Post, J.L., Stoffregen, R.E. and Ashley, R.P. (2014) Mapping
874 advanced argillic alteration at Cuprite, Nevada using imaging spectroscopy. *Economic*
875 *Geology*, 109, no. 5, p. 1179-1221. DOI:10.2113/econgeo.109.5.1179

876 Thollot, P., et al. (2012) Most Mars minerals in a nutshell: Various alteration phases formed in a
877 single environment in Noctis Labyrinthus, *Journal of Geophysical Research*, 117,
878 E00J06, doi:10.1029/2011JE004028.

879 Tosca, N. J., McLennan, S. M., Lindsley, D. H., and Schoonen, M. A. A. (2004), Acid-sulfate
880 weathering of synthetic Martian basalt: The acid fog model revisited, *Journal of*
881 *Geophysical Research*, 109, E05003, doi:10.1029/2003JE002218.

882 Vaniman, D. T., et al. (2014) Mineralogy of a mudstone on Mars, *Science*, 343, 6169,
883 doi:10.1126/science.1243480.

884 Varekamp, J.C. et al. (2009) Naturally acid waters from Copahue volcano, Argentina. *Applied*
885 *Geochemistry*, 24, 208-220.

886 Wang, A., et al. (2008) Light-toned salty soils and coexisting Si-rich species discovered by the
887 Mars Exploration Rover Spirit in Columbia Hills, *Journal of Geophysical Research* 113 ,
888 E12S40, doi:10.1029/2008JE003126

889 Weitz, C.M., Milliken, R.E., Grant, J.A., McEwen, A.S., Williams, R.M.E., Bishop, J.L. and
890 Thompson, B.J. (2010) Mars Reconnaissance Orbiter observations of light-toned layered

891 deposits and associated fluvial landforms on the plateaus adjacent to Valles Marineris.
892 Icarus doi:10.1016/j.icarus.2009.04.017, 2010.

893 Weitz, C. M., et al. (2011) Diverse mineralogies in two troughs of Noctis Labyrinthus, Mars,
894 Geology, 39(10), 899–902, doi:10.1130/G32045.1

895 Wray, J. J., et al. (2011) Columbus crater and other possible groundwater-fed paleolakes of Terra
896 Sirenum, Mars, Journal of Geophysical Research, 116, E01001,
897 doi:10.1029/2010JE003694.

898 Zolotov, M.Y. and Mironenko, M. V. (2014) Massive sulfate deposits on Mars could be
899 remobilized Noachian salts. 45th Lunar and Planetary Science Conference, March 17-21,
900 2014, The Woodlands, TX, abstract 2876

Figure captions

901
902
903
904
905
906
907
908
909
910
911

912
913
914
915
916
917
918

919
920
921
922

Figure 1. (a) Location of Cross crater on a MOLA topographic map of Mars where red colors are high elevations and blue are low elevations. Elevation range is approximately -2500 m to 10,000 m. (b) MOLA topographic map of Cross crater overlain on CTX. (c) Nighttime thermal infrared map from THEMIS (Christiansen et al., 2004). Bright-toned areas are warmer and higher thermal inertia. Peak ring materials and bright sedimentary layers are relatively lower thermal inertia relative to a later emplaced dark cap rock. (d) CRISM multispectral maps showing the locations of secondary minerals within and around Cross crater using band depth parameterizations (Pelkey et al., 2007). Red: BD1900 for H₂O in mineral structures, Green: BD2200 for Al-OH and Si-OH, Blue: BD2300 for Fe-OH and Mg-OH.

Figure 2. Spectra of alunite-bearing materials (red), alunite- and kaolin-bearing materials (yellow), kaolin-bearing materials (blue), and silica or Al-smectite-bearing materials (green) from Cross crater CRISM image FRT0000987B compared to library spectra. The low-temperature lacustrine alunite spectrum was acquired of samples from Lake Tyrrell, Australia, and the hydrothermal alunite spectrum was of samples from Marysvale, Utah. The opaline silica acquired under Mars pressure and temperature conditions is from Swayze et al. (2007). All other library spectra are from the Clark et al. (2007) reference database.

Figure 3. Tetracorder maps of CRISM images in Cross crater, showing the spatial distribution of the aluminous endmembers and their mixtures. Colors correspond to the colors of spectra in Figure 2 and images used in the mapping are listed in Table 1 and indicated here by their image IDs with leading zeros removed.

923 **Figure 4.** (a) Fe/Mg-phyllsilicates within Cross crater are found in the rim of a small interior
924 crater as well as at the outer margins of its ejecta blanket. Band depth maps at 2.3 μm from
925 CRISM images FRT0009878 and FRT0000ACE6 were overlain on CTX image
926 P15_006945_1494_XN_30S158W_080119 and displayed where values >0.0 . There is some
927 residual striping from detector artifacts in the mineral map. White, circled regions have Fe/Mg-
928 phyllosilicates; spectra are shown in panel c. A context map for the location is in Figure 3. (b)
929 Example of a friable, Fe/Mg phyllosilicate deposit identified in CRISM mapping data shown in
930 CTX image P20_009028_1495_XI_30S157W_080629. Spectra from the white, circled area are
931 shown in panel c. A context map for the location is in Figure 1d. (c) spectra from the locations in
932 (a) and (b) compared to laboratory measurements of nontronite, an Fe-smectite, and saponite, an
933 Mg-smectite (Clark et al., 2007).

934 **Figure 5.** (a) Context for a MOLA profile of Tetracorder maps on CTX from the southeastern
935 part of Cross crater. The white box shows a portion of (c). (b) MOLA point shot data show the
936 alunite/kaolinite-bearing units form a distinctive bench with topographically lower silica or
937 montmorillonite deposits. (c) Tetracorder maps on CTX from the southwestern part of Cross
938 crater showing the morphology of mineral-bearing units. (d, e) alunite units are massive beneath
939 dark materials in HiRISE PSP_008883_1490_RED. Silica-bearing units are fractured at (f) km-
940 scale and (g) meters-scale in HiRISE ESP_016320_1490_RED. The silica bearing materials
941 occur beneath a dark cap rock.

942 **Figure 6.** Finely layered Al-phyllsilicate-bearing Cross crater sedimentary materials in (a)
943 northwestern Cross crater in ESP_013274_1495_RED, (b) northern Cross crater in
944 PSP_010584_1500_RED,, and (c) southern Cross crater in PSP_010228_1490_RED. Eroded
945 Cross crater sediments have two characteristic types of layering, typified, respectively, by (a, c)

946 and the more spatially widespread (b). (d) a 3D perspective view of the southern wall of Cross
947 crater shows the eroded topography and how the most alunite-enriched area has a distinct lack of
948 bedding. HiRISE digital elevation model from PSP_010228_1490 and ESP_016320_1490.

949 **Figure 7.** (a) MOLA topographic image of Cross crater with color gradient across the
950 topographic range subset to emphasize topography in the vicinity of Cross crater. The range
951 shown is from approximately 600m to 2600 m above the MOLA datum. (b) Zoom of (a)
952 showing the eastern inlet valley and a putative inlet valley into Cross crater. (c) Topographic
953 profile across the valley. (d) A CRISM mineral map tracking the depth of an absorption near
954 2.17-2.20 μm . The strongest signatures are within Cross crater in sediments. Four locations along
955 the inlet valley, 200 m higher in elevation, also exhibit absorptions characteristic of aluminous
956 materials. HiRISE images from (e) ESP_012641_1495_RED and (f) ESP_033383_1495_RED
957 show the outcrops of materials in the valley at finer spatial resolution. (g) CRISM spectra from
958 FRT00014744 at the four locations.

959 **Figure 8.** Predominance area diagrams to illustrate geochemical conditions favorable for alunite
960 kaolinite, and jarosite. Concentration of dissolved species and co-existing solid phases were
961 based on simulated reaction of terrestrial volcanic gas compositions (Symonds et al., 2004) with
962 Martian basaltic composition (Poulet et al. 2009). (a) Plot of Al phases as a function of pH and
963 sulfate activity. Alunite is favored at pH lower than kaolinite and with increasing sulfate activity.
964 (Diagram calculated at: $T=5^\circ\text{C}$, $P=0.5$ bars, $a\text{Mg}^{2+}=10^{-3}$, $a\text{K}^+=10^{-5}$, $a\text{Ca}^{2+}=10^{-3}$, kaolinite,
965 $\text{SiO}_2(\text{am})$ and $\text{Fe}(\text{OH})_3(\text{am})$ have $a = 1$; pyrophyllite, jurbanite, laumontite is suppressed). (b)
966 Plot of sulfate phases as a function of pH and the ratio of $\text{Al}^{3+}/\text{Fe}^{3+}$, which must be high to favor
967 alunite. ($T=5^\circ\text{C}$, $P=0.5$ bars, $a\text{Mg}^{2+}=10^{-3}$, $a\text{K}^+=10^{-5}$, $a\text{SO}_4^{2-} = 10^{-2}$, $a\text{Ca}^{2+}=10^{-3}$; $\text{SiO}_2(\text{am})$ and
968 $\text{Fe}(\text{OH})_3$ have $a = 1$; jurbanite, and basaluminite are suppressed) C. Superimposed predominance

969 diagrams for Fe and Al phases as a function of pH and fO_2 . ($T=5^\circ\text{C}$, $P=0.5$ bars, $aMg^{2+}=10^{-3}$,
970 $aK^+=10^{-5}$, $aSO_4^{2-}=10^{-2}$, $aCa^{2+}=10^{-3}$; $SiO_2(am)$, $Fe(OH)_3(am)$, and kaolinite have $a=1$; jurbanite,
971 laumontite, pyrophyllite, goethite, and hematite are suppressed). Diagrams calculated using
972 Geochemist's Workbench v.8.0 using the Wateq4 database.

973

974
975
976
977
978
979
980
981
982

Tables

Table 1. CRISM full- and half-resolution images used in this study. Images are listed clockwise around the crater, starting at the inflow valley on the east. Coverage is duplicative in some cases. The best images used for Tetracorder mapping (see Datasets & Methods) are indicated. An asterisk on the image ID indicates data that are short wavelength only, i.e., acquired from 0.4-1.0 μm rather than 0.4-4.0 μm . All CRISM images as well as a map of the image footprints are available at the NASA PDS Geosciences Node website.

CRISM Image ID	Day-of-year	Used in Tetracorder mapping (Fig. 3)
FRT00014744	2009_230	
FRT00011E7D	2009_097	
FRT0000B49F	2008_181	yes
HRL00012386	2009_113	
FRT00019DFE	2010_201	
FRT00021B59	2011_338	
FRT00010AE2	2009_025	
FRT0000D24B	2008_303	yes
FRT00012E09	2009_146	
FRT0000ACE6	2008_136	yes
FRT0000B252	2008_170	yes
FRT0000987B	2008_019	yes
FRT0001EF51*	2011_189	
FRT0001DABB	2011_101	
FRT0001187B	2009_069	
FRT0000CC44	2008_275	yes
FRT000137C2	2009_185	yes

983
984

985

Figures

986

987

988

Figure 1

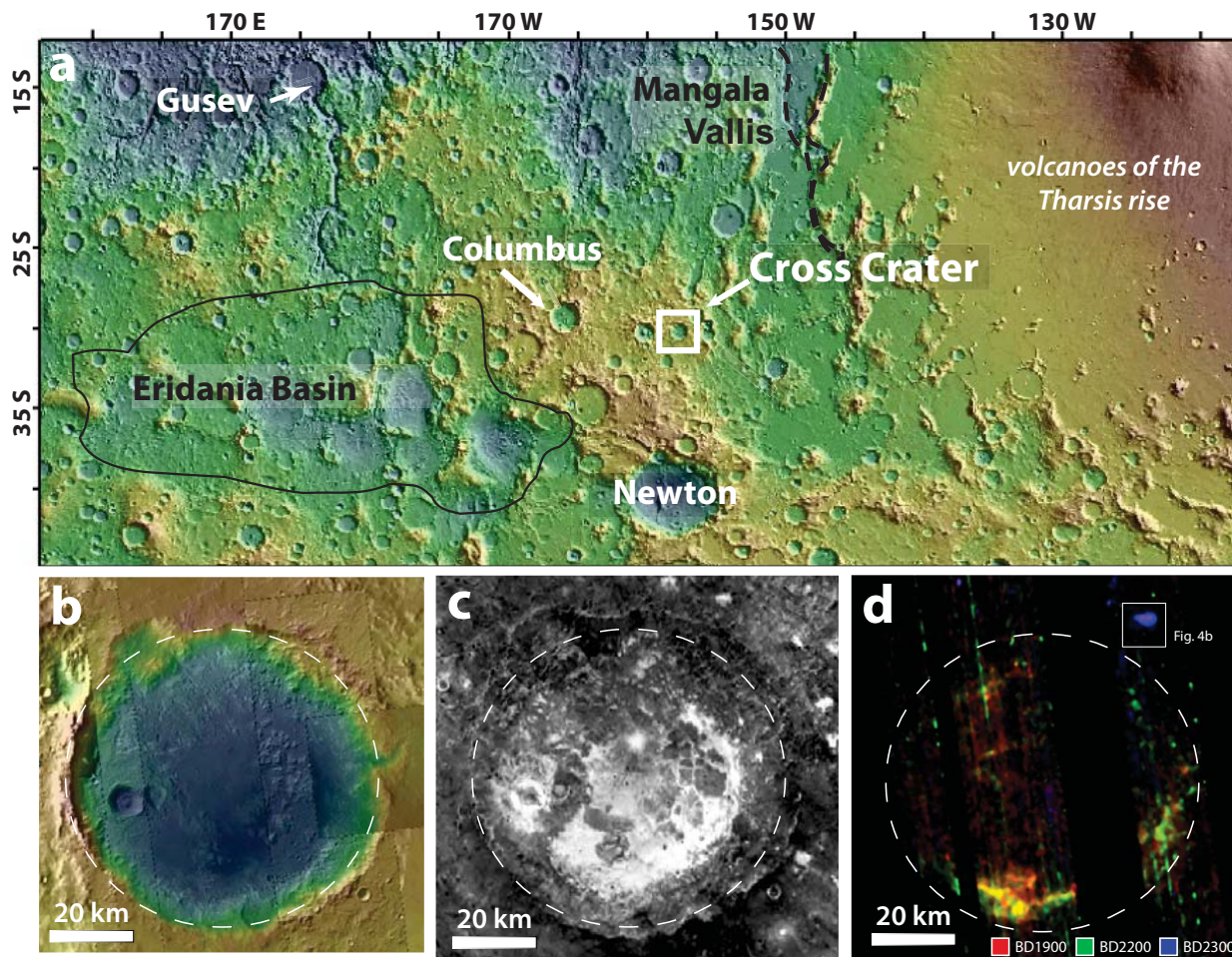
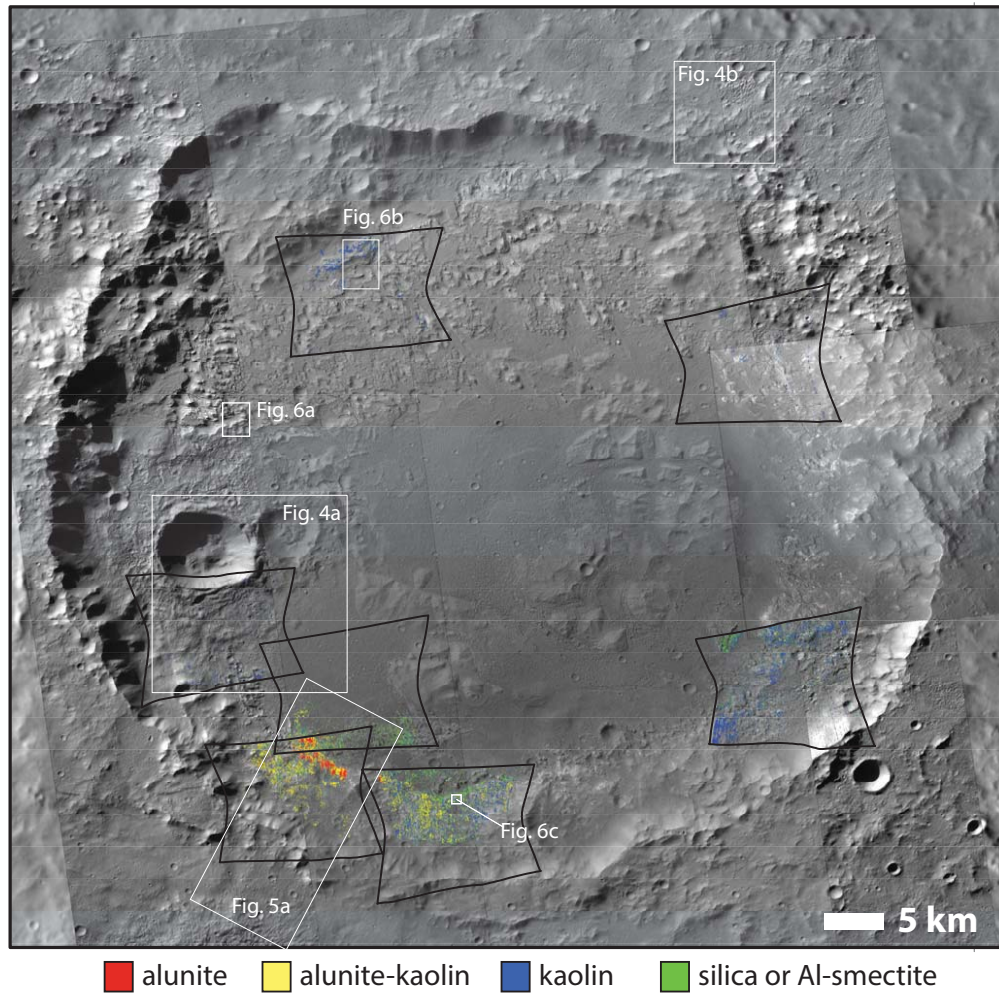


Figure 3



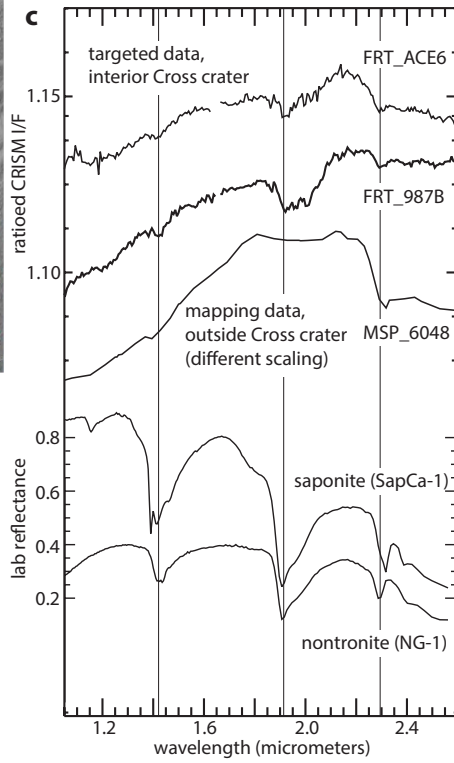
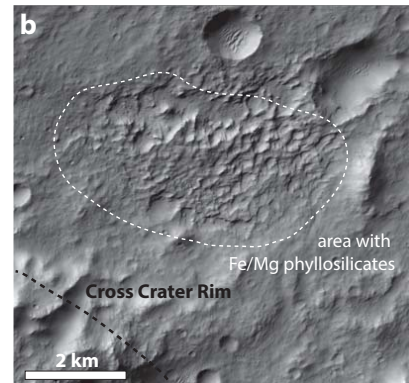
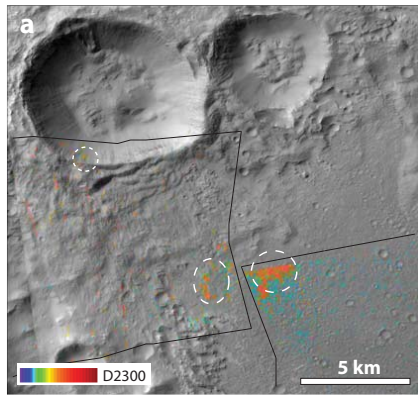


Figure 5

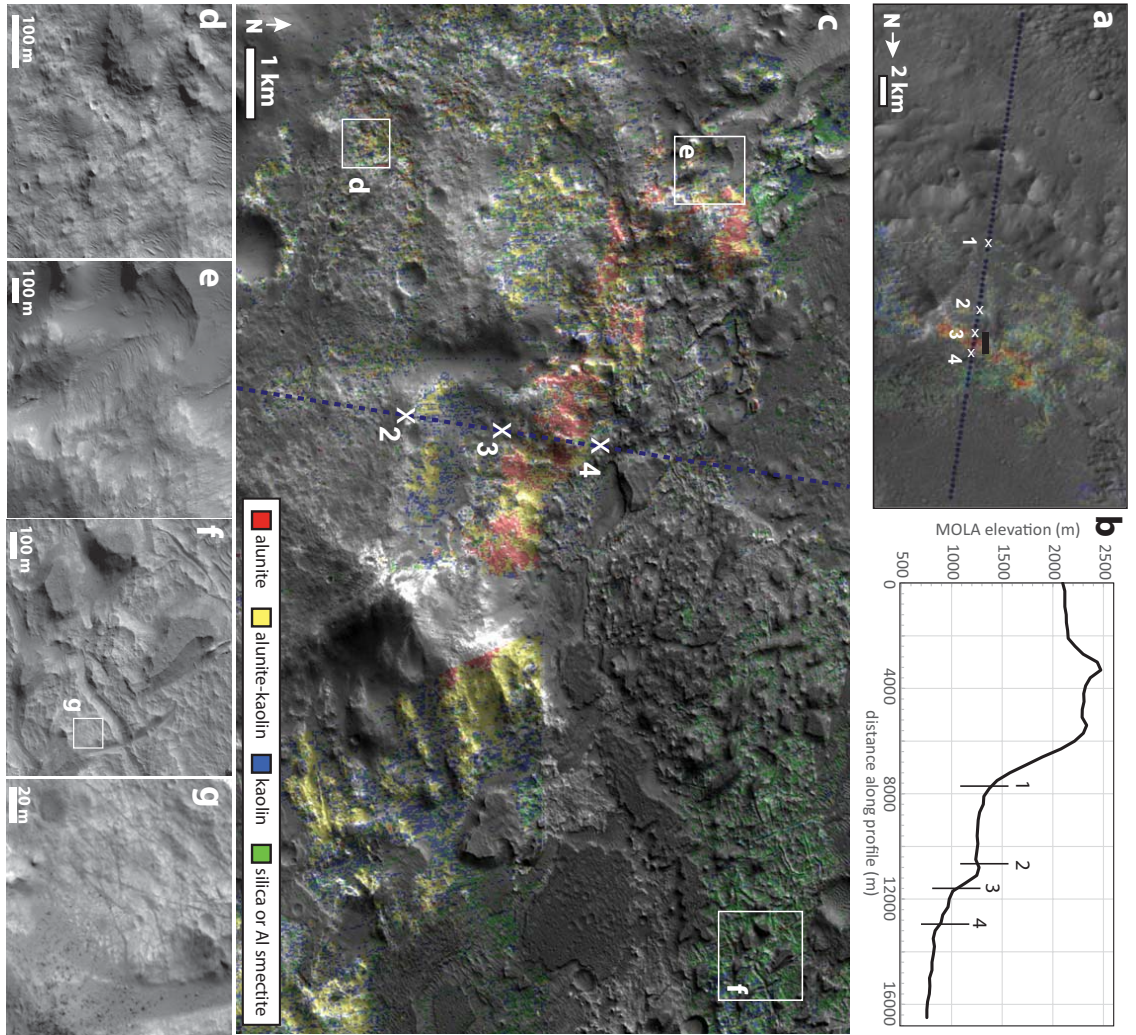


Figure 6

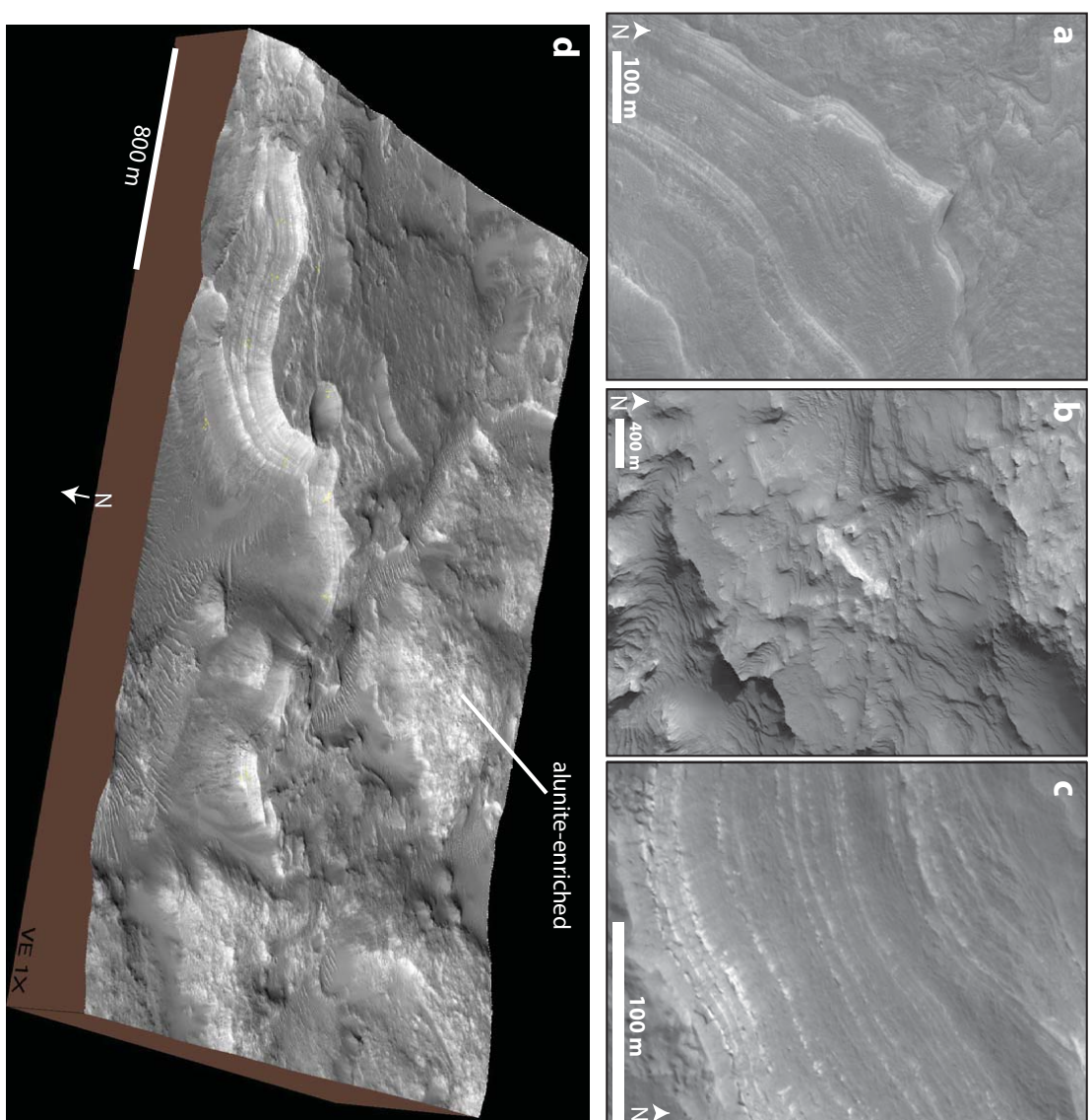


Figure 7

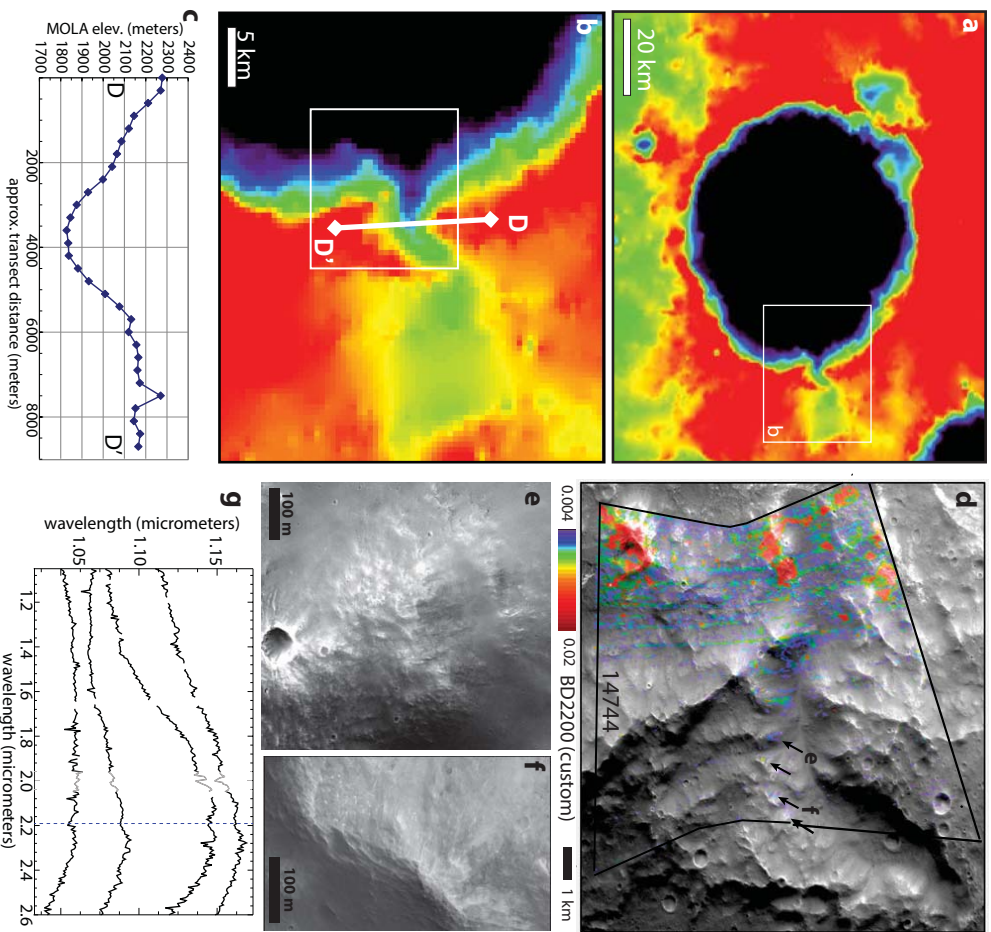


Figure 8

